MINIMIZATION OF INHOMOGENEITIES IN MAGNETIC RESONANCE MAMMOGRAPHY

by

Orkun Serdar Doğruluk

B.S., E.E., Yıldız Technical University, 2002

Submitted to Institute of Biomedical Engineering

in partial fulfillment of the requirements

for the degree of

Master of Science

in

Biomedical Engineering

Boğaziçi University

February 2006

ACKNOWLEDGMENTS

There are a number of people without whom this thesis would not been possible. I would like to thank to my supervisor Assoc. Prof. Dr. Halil Özcan Gülçür for his support, assistance and great patience. His guidance leads me to finish this work. I also would like to thank my jury members, Prof. Dr. Yekta Ülgen and Prof. Dr. Osman Nuri Uçan. I also would like to thank Gökhan Ertaş for his support and assistance. His ideas and our discussions on this topic gave me another way of looking and problem solving. I also would like to thank my family and my friends who always encouraged me to finish this work.

ABSTRACT

MINIMIZATION OF INHOMOGENEITIES IN MAGNETIC RESONANCE MAMMOGRAPHY

Magnetic Resonance Mammography (MRM), accepted by for use as a supplemental tool to mammography in 1991, provides detailed information about very small lesions that X-ray mammography and ultrasound often cannot detect. Women who are at increased risk for developing cancer, or those who have completed breast conserving "lumpectomy", young women with dense breasts or those with a great amount of DCIS (ductal carcinoma in situ) are good candidates for MRM.

Resolution of the breast imaging is important for improving differentiation between benign and malignant lesions and for refining treatment strategy. Inhomogeneity of the static magnetic field or secondary magnetic field and nonuniformity of the receiver coil have adverse effects on resolution. A number of methods have been proposed to minimize these effects. In this thesis work we present a novel improved homomorphic filtering method to minimize artifacts caused by these inhomogeneities. Unlike other homomorphic filtering methods, we apply a tissue mask to eliminate filter artifacts, and then apply low-pass filtering to estimate the bias field. Restored image is obtained by the difference of the original image and the estimated bias field. A frequency range is defined and a number of bias fields and restored images are estimated for each image. Entropy minimization is used to define an optimum cutoff frequency of the low-pass filter. This results in a fast, user independent, nonparametric algorithm. The method is demonstrated on various breast images from different patients. A performance evaluation method is also defined for quantitative measurement.

Keywords: Magnetic resonance mammography, field inhomogeneity; homomorphic filtering, entropy minimization

ÖZET

MANYETİK REZONANS MAMOGRAFİSİNDE DÜZENSİZLİKLERİN EN AZA İNDİRGENMESİ

Manyetik rezonans mamografisi (MRM), X-ışınlı mamografi ve ultrases ile belirlenemeyen çok küçük lezyonlar hakkında ayrıntılı bilgi vermesi nedeniyle geleneksel mamografiye yardımcı bir araç olarak 1991 yılından beri kullanılmaktadır. Yüksek kanser oluşturma riskine sahip kadınlar, meme dokusunun tamamının alınmadığı lumpektomi ameliyatı geçirenler veya yüksek miktarda DCIS (ductal carcinoma in situ) içeren yoğun meme dokusuna sahip kadınlar MRM için uygun hastalardır.

Meme görüntülerinin çözünürlüğü gerek iyi huylu ve kötü huylu lezyonların ayırt edilmesi gerekse uygun tedavi yöntemlerinin belirlenmesi açısından oldukça önemlidir. Duruk ve ikincil manyetik alanların homojen olmaması ve alıcı sarımdaki düzensizlikler çözünürlük üzerinde olumsuz sonuçlara neden olur. Bu etkiyi azaltmak için çeşitli yöntemler önerilmiştir. Bu tez çalışmasında belirtilen düzensizliklerden kaynaklanan etkileri azaltmak için yeni bir gelişmiş homomorfik süzme yöntemi önerilmiştir. Diğer homomorfik süzme yöntemlerinden farklı olarak, süzmeden kaynaklanan sorunları engellemek amacıyla bir doku maskesi uygulanmış ve sapma alanı alçak geçiren süzgeç yardımıyla belirlenmiştir. Enuygun görüntü görüntü elde edilen sapma alanının, çekim sonucu elde edilen görüntüden çıkarılmasıyla bulunur. Süzgeçleme için bir frekans aralığı belirlenmiş ve farklı kesme sıklıkları için belirli sayıda sapma alanı ve enuygun görüntü elde edilmiştir. Entropi azaltma yöntemi, alçak geçiren süzgeçin enuygun kesme sıklıklarını belirlemek amacıyla kullanılmıştır. Bu yöntem hızlı, kullanıcıdan ve parametrelerden bağımsız bir algoritma oluşturmaktadır. Yöntem farklı hastalardan alınan görüntüler üzerinde denenmiştir. Ayrıca yeni bir nicel başarım çözümleme yöntemi önerilmiştir.

Anahtar kelimeler: Manyetik rezonans mamografisi, alan düzensizlikleri, homomorfik süzgeçleme, entropi

TABLE OF CONTENTS

LIST OF FIGURES

LIST OF TABLES

LIST OF SYMBOLS

σ_t^2	Overall variance
σ_b^2	Between-classes variance
σ_w^2	Within-class variance
t	Optimum threshold
μ_t	Overall mean of all pixels
$\eta(t)$	Ratio between-class variance to total variance
f_c	Cutoff frequency
E	Average information loss

LIST OF ABBREVIATONS

MRM	Magnetic Resonance Mammography
DCIS	Ductal Carcinoma in Situ
RF	Radio Frequency
MR	Magnetic Resonance
US	Ultrasound
GE	Gradient Echo
TSE	Turbo Spin Echo
CSF	Cerebro Spinal Fluid

1. INTRODUCTION

1.1 Background and Motivation

The incidence of breast cancer is slowly increasing worldwide. In developed nations women have a lifetime breast cancer risk of approximately 1 in 12. With the introduction of mammographic breast screening programs, the incidence has increased in the last 10 years, but this change has been accompanied by a shift to smaller lesions and by a marked increase in the detection of ductal carcinoma in situ (DCIS). In combination with earlier detection, improved and adjuvant treatments have actually resulted in a decline in breast cancer mortality rates in some countries in the last decade [1]-[3].

Although the breast was one of the first organs studied with MRI for the detection of cancer, and it was also the first organ in which the detection of invasive tumor neovascularity was highlighted through the application of rapid serial imaging after an injection of contrast agent, currently it is not the first clinical choise for initial breast screening. Conventional breast assessments are based on the combination of screen-film X-ray mammography, high-resolution breast ultrasonography (US), and clinical breast examination. These methods are used to detect approximately 85-90% of breast malignancies. Despite their usefulness however, these conventional methods may fail to depict a breast malignancy accurately in the following stiutations:

1. Palpable lesion without a focal imaging correlate,
2. interval cancers that are missed or not visible on initial images,
3. understaging of the extent of the lesion or multifocality in the same or opposite breast,
4. patient presenting with distant or axillary breast cancer metastasis with no breast lesion found on mammograms or sonograms,
5. inaccurate clinical assessment of large tumors that are treated with neoadjuvant chemotherapy,
6. chest wall invasion that is not detected.

Magnetic resonance mammography (MRM) has been shown to be a sensitive and effective method of detecting, diagnosing, and staging intramammary breast malignancy, even when conventional imaging results have been negative as in the above situations. Because of this ability to depict malignancies that are otherwise not visible, MRM has been the subject of active research and development around the world, and its use for certain specific indications has been accepted. The technical developments that revolutionized breast MRI and made it an important adjunct technique for the evaluation of breast disease include the following:

1. Development of the intravenous (IV) contrast medium for MRI, (gadolinium dimeglumine, in the early 1980s),
2. development of rapid GRE pulse sequences sensitive to contrast enhancement (mid-1980s),
3. development of high-field-strength magnets (>1 T) that enabled spectral fat-suppression techniques,
4. development of dedicated breast coils for bilateral or independent breast imaging,
5. exploitation of new methods of *k*-space filling to increase speed and resolution, (from the mid-1990s to the present),
6. development of computerized automated techniques of contrast enhancement, and
7. architectural feature analysis for large image datasets.

Despite its advantages, MR images can be corrupted by several artifacts which may show up as anatomically irrelevant intensity variations throughout data. They can be induced by a variety of factors, including the following [1],[2]:

1. Non-uniformity of the B0 static field[1],
2. Non-linearity of the gradient fields,
3. Imperfections in the geometry and the physical properties of the RF coil,
4. Problems with the coil tuning, and focusing problems[2],

[1] Local variations in B_0 are compensated by shim tuning, any uncompensated in B0 may lead to a local artifacts in the acquired image.

[2] Especially when a large number of echoes are acquired.

5. Intensity variations in the spin echo and gradient echo pulse sequences[3],
6. Eddy currents which are triggered when the field gradients are switching[4],
7. Noise and/or nonlinearity problems in the electronic circuitry (amplifiers and digital-to-analog converters), and
8. Complex electromagnetic interactions between the imaged object (tissue) and the acquisition system[5] .

1.2 Objectives

Resolution of the breast image is important for improving discrimination between benign and malignant lesions and for refining treatment strategy. Unfortunately MRM datasets can be corrupted by artifacts which may show up as anatomically irrelevant intensity variations throughout the MRM image due to a number of factors, including non-uniformity of the B0 static field, non-linearity of the gradient fields, imperfections in the geometry and the physical properties of the RF coil, problems with the coil tuning, focusing problems, intensity variations in the spin echo and gradient echo pulse sequences, eddy currents which are triggered when the field gradients are switching, noise and/or nonlinearity problems in the electronic circuitry, and complex electromagnetic interactions between the imaged object (breast tissue) and the acquisition system. A number of methods have been proposed to minimize the "inhomogeneity" caused by the aforementioned artifacts within the acquired MR images. However, most of these techniques require either user interaction and/or prior tissue information and have been specifically developed for brain MR images; a correction scheme developed especially for breast MR images. Therefore, the objective of this thesis is to decelop an effective method to correct MRM images, which is non-parametric and user independent.

---

[3] For Spin Echo pulse sequences it has been shown that interleaved acquisitions perform better in terms of intensity non-uniformity.

[4] This effect will be pronounced especially when the repetition time (TR) is small.

[5] The shape and the physical characteristics of the imaged object has a significant effect on intensity non-uniformity due to complex electromagnetic interactions.

1.3 Outline of the Thesis

Chapter 1 introduces the subject, presents the motivation of the thesis and gives an outline. Chapter 2 is a brief discussion on current breast imaging techniques. The method used in the thesis is discussed in Chapter 3. It gives information about homomorphic filtering, how to obtain a tissue mask and how to construct homomorphic filters. Entropy minimization and application details are presented in this chapter. Basic results of this research work on various MR images obtained from patient scans are presented in Chapter 4. Image quality definitions and measurement of information lost during processing are also discussed in this chapter. Chapter 5 includes a summary of the basic results and a detailed discussion.

2. BREAST IMAGING TECHNIQUES

2.1 Mammography

Mammography, with its sensitivity in screening of 90–93% and specificity of 93–97% is one of the basic imaging methods used in breast diagnostics. The aim of interpreting mammograms is to find some, if any, indicators for breast malignancy such as asymmetric densities, mostly circular or stellate lesions; parenchymal contour changes; architectural distortion and micro calcifications [1].

Mammography has some recognized limitations and disadvantages. The sensitivity and specificity are highly dependent on the composition of the breast parenchyma, which for its part is influenced by age, hormonal status and possible previous interventions. In young women, the usefulness of mammography is restricted by high prevalence of dense fibroglandular tissue, which impairs both the detection and the differentiation of the lesion. With increasing age, the breast parenchyma usually shows fatty replacement, which makes abnormalities more easily detectable [4].

2.1.1 Digital mammography

Digital mammography has the potential to overcome some of the limitations of conventional mammography. Because of the increased contrast and decreased noise of digital systems, it is possible to improve image quality. However the spatial resolution is still limited when compared to screen-film mammography. The possibilities for image post-processing reduce the need for repeats and additional (e.g. magnification) views, which also enables radiation dose reduction [4].

2.1.2 Other mammographic techniques

In case of spontaneous nipple discharge, galactography has been the method of choice. A mammogram taken after duct cannulation and contrast injection reveals possible intraductal tumors as filling defects, and with the same method, the lesion can also be preoperatively marked with methylene blue dye. Galactographic finding helps to localize the origin of nipple discharge but is nonspecific. Sometimes cannulating a

secreting duct may be impossible. The latest high-resolution ultrasound machines allow visualization of the dilated ducts and the intraductal tumors [1]-[3].

2.2 Ultrasonography

2.2.1 B-mode ultrasonography

Ultrasonograpy (US) has been used in breast diagnostics since the 1950s. Until recently, the main indications of breast US have been differentiation between cystic and solid lesions, evaluation of a palpable lesion in a mammographically dense breast (for example young, pregnant or lactating patient), evaluation of a lesion detected at mammography or mammographic asymmetry, detection of an abscess in an infectious breast, evaluation after breast cancer treatment and breast augmentation, evaluation of axillary lymph nodes and guidance for interventional procedures [4].

Ultrasound can detect mammographically occult cancers, but it is generally accepted that US is not suitable for screening. Micro calcifications with no associate mass are not usually reliably detectable at US, although demonstration of micro calcifications by the latest high-frequency techniques has been published. The analysis of micro calcifications is, however, only possible with mammographic spot magnification [4].

2.2.2 Doppler techniques

In the Doppler Effect, the sound waves reflected from a moving medium undergo a frequency shift, which is used to image red blood cells moving within vessels and to measure their velocity. The Doppler shift is proportional both to the flow velocity and the transmission frequency of the ultrasound. In color Doppler ultrasound, the Doppler signals received from flowing blood are processed and color-encoded. The velocities are displayed in various colors and brightness levels. The color-encoded flow information is superimposed onto the B-mode image in real time. The more recent power Doppler gives also color-encoded information, but it analyzes the amplitude of the reflected signal, not the frequency shift. The amplitude depends on the quantity or density of the blood cells that are detected. The signal-to-noise ratio is better with power

Doppler, which enables more accurate detection of the small tumor vessels than conventional color Doppler [1].

A considerable problem in tumor diagnostics is that the spatial resolution of Doppler imaging is limited, and only major feeding vessels of the tumors are detectable, not the abnormal complex micro vascularity. Color Doppler, or even the more sensitive power Doppler, is not capable of detecting the flow information in small vessels in all directions. The technique is also equipment and operator dependent. Neither examination techniques nor interpretation of the Doppler images are standardized and the results of the studies vary considerably [1].

2.2.3 Contrast-enhanced ultrasonography

The finding that Doppler signals may be difficult to detect either because of small vessel size or inadequate equipment has led to the development of ultrasound contrast agents. They are encapsulated micro bubbles, which increase the acoustic scattering from the tissues through which they pass. Because US contrast agents do not extravagate from the vessel to the surrounding tissue, any echo received indicates the presence of a vessel. Contrast enhancement improves detection of small vessels with slow and low-volume blood flow. It reduces equipment dependence and could theoretically improve standardization by also providing dynamic flow information, which can be quantified [4].

2.3 Computed Tomography

Computed tomography has not been recommended for breast imaging, mainly because of high radiation dose. It has been successfully used in regional staging of small breast cancer before breast conserving surgery [4].

2.4 Electrical Impedance Scanning

Electrical impedance scanning is a new technique, which is based upon the principle that malignant cells exhibit altered local dielectric properties and show measurably higher conductivity values. The method has been presented as a useful tool

for further evaluation of equivocal mammographic findings, but its real value remains to be seen [4].

2.5 Nuclear Medicine

The most important task of nuclear medicine with regard to breast cancer is nowadays sentinel node staging using lympho-scintigraphy. In differential diagnostics, nuclear medicine is under investigation as an adjunct to mammography. Positron emission tomography scanning might have a role in differential diagnosis and in staging of breast tumors [1]-[4].

2.6 Magnetic Resonance Imaging

2.6.1 Background

The capabilities of MR imaging in breast imaging have been investigated since the 1970s. With the introduction of contrast agents and the first encouraging results of contrast-enhanced MR imaging in the 1980s it emerged as a promising modality for breast diagnostics [4].

MR imaging has proved to be the most sensitive method for the detection of invasive breast cancer. The detection is based on lesion enhancement after contrast agent administration. In various series, the sensitivity for invasive breast cancer has ranged from 88 to 100%, and the specificity from 37 to 97% [3], [4].

2.6.2 Technique

There is no universally accepted standard or optimal technique for breast MR imaging. One thing is generally accepted: intravenous contrast enhancement is essential. There is always a compromise between temporal and spatial resolution in MR imaging. Some investigators emphasize temporal resolution to follow enhancement kinetics in breast lesions, while others consider spatial resolution to be more important at the cost of temporal resolution. With newer equipment, however, it is possible to obtain higher spatial resolution even during dynamic scanning. Most investigators have used high-field - strength (1.0–1.5 T) imaging systems. A dedicated bilateral breast coil and prone

position of the patient are preferable. The whole affected breast as well as the contralateral breast should be imaged simultaneously. The sequences used usually include at least T1-weighted images before and after contrast agent administration. For the dynamic series, fast gradient echo (2- or 3-dimensional) sequences with a temporal resolution ≤ 2 minutes are recommended. The contrast agent used is Gd-DTPA (gadolinium diethylene triamine pentaacetic acid) with a dose of 0.1–0.2 mmol/kg body weight intravenously. To get good spatial resolution, slice thickness ≤ 3 mm with no gaps is recommended. Fat suppression, or when fat suppression is not used, post-processing with image subtraction is essential in the detection of pathological enhancement. Patient motion reduction is an important issue, too, especially when image subtraction is used for lesion detection. Beyond these general guidelines, there is a great deal of variation in other imaging parameters (orientation, field of view, time of acquisition, imaging matrix etc.) [4].

2.6.3 Indications and contraindications

Most breast lesions can be diagnosed by using conventional modalities, especially when combined with needle biopsies. It is, however, desirable to be able to reduce the number of biopsies performed for benign causes. In dealing with lesions that remain equivocal after mammographic and sonographic evaluation, MR imaging could be the problem-solving method. A negative MR imaging finding virtually excludes invasive carcinoma.

The aim of breast imaging is the detection of breast cancer as early as possible, as the prognosis of breast cancer depends on the stage of the disease at the time of diagnosis. MR imaging is not considered suitable for breast screening in a general population, but it might be feasible in imaging the extremely dense breasts of especially young high-risk women (family history, cancer susceptibility genes, and history of contralateral breast cancer). It is the best method for detecting an otherwise occult primary breast carcinoma in patients with axillary node metastases. After a cancer diagnosis, MR imaging is the most sensitive tool for preoperative staging and treatment planning. MR imaging can also be an adjunctive method in post treatment surveillance in conservatively treated breasts with suspected recurrence and evaluation of tumor

response to chemotherapy. MR imaging is also the best method for imaging of breasts with silicon prostheses [4].

In addition to general contraindications for MR imaging (e.g. cardiac pacemaker, ferromagnetic incorporated substances) there are some specific limitations concerning breast imaging. It must not be used instead of x-ray mammography, because according to present knowledge, it is not suitable for detecting and evaluating micro calcifications. Due to its variable specificity, MR imaging should not be used for imaging symptomless women without an increased risk of breast cancer. Before breast MR imaging can be a clinically used tool for breast imaging, a proper MR-guided biopsy and localization system must be available for biopsy of suspicious lesions not detected by other modalities. The verification of lesion removal is also a major problem to solve, because MR imaging of the excised specimen is not feasible [4].

2.6.4 Low-field versus high-field magnetic resonance imaging

There are no strict criteria for classifying MR-scanners as high-field or low-field. Usually, the scanners with field strength of 1.0 T or higher are considered high-field, and those with field strength of 0.2 T or lower are considered low-field. Scanners between these limits are called mid-field. The 0.23 T MR-scanner used in the present study is considered low-field, although it exceeds the limit of 0.2 T [4].

Practically all of the breast MR imaging studies have been performed with high-field systems. The results of the few studies with low-field (0.02–0.1 T) scanners almost 10 years ago were not very satisfactory. Nowadays the technique is more advanced, but there are still no comparative breast studies between low-field and high-field MR-scanners. The main disadvantage of low-field MR imaging is the poor signal-to-noise ratio, which has to be compensated by a lower imaging bandwidth. This in turn results in a longer acquisition time and a risk of motion artifacts. The spatial resolution is limited, too. As the T1 relaxation times of tissues are shortened in low-field compared to high-field scanners, contrast enhancement, which also decreases the T1 times, causes less difference between the tissues in low-field than in high-field systems. This may lead to misdetection of enhancing lesions. Moreover, all the pulse sequences routinely used in high-field systems are not available in low-field imagers. This leads to

compromises in imaging techniques. In low-field MR imaging there is not enough frequency shifts between fat and water protons, which prohibit the use of chemical shift fat saturation technique. A method based on the phase difference between fat and water protons has been developed, which might also be useful in breast MR imaging. Low-field scanners do, however, provide some advantages, like cost savings and lesser space requirements, which have raised the interest in using them in routine imaging. The open architecture provides more potential for interventional procedures. In imaging, chemical shift, susceptibility and flow artifacts are less obvious than in high-field systems [4].

2.6.5 Dynamic MR imaging of the breast

Breast MRI can be divided into two phases: morphological and dynamic. Morphological imaging includes both T1 and T2 sequences on the axial and/or saggital planes. It is performed with T1 GE (Gradient Echo) and T2 TSE (Turbo Spin Echo) sequences and aims at identifying the site, shape, and margins, solid or liquid content of a lesion and its relationship with surrounding structures [1]-[4].

Dynamic imaging includes rapid 2D or 3D GE sequences and intravenous contrast administration. It is performed to obtain data for the differential diagnosis between malignant and benign lesions based on the vascular enhancement pattern. It requires extremely rapid acquisitions (under 1 min) since enhancing lesions are visualized in the first 60 – 90 sec [4].

Today the best available rapid sequences in terms of spatial resolution are 3D GE. To identify lesions isointense to fat, the signal from fat is suppressed by image subtraction to enhance the detection potentials of these sequences.

Rapid GE images are acquired before contrast administration and afterwards for 5 – 12 min. The slice where the lesion is the best depicted is then selected and all the images of that slice are studied; a region of interest is placed on the lesion and the enhancement curve over time is drawn [1]-[4].

2.6.6 RF Inhomogeneity or bias field

RF inhomogeneity or bias field is defined as slowly changing and smooth spatial variations of the same tissue over the image domain [5, 6]. The sources of bias field vary, but is usually related to the inhomogeneity of the static magnetic field, $B_{0,}$ of the MR system; inhomogeneity of the radiofrequency (RF) pulse generated by the oscillating secondary magnetic field, B_1 (which is caused by the nonuniformity of the RF generating transmitter coil or distortion of the RF field by the object being scanned); or nonuniformity of the receiver coils used to detect the MR signal [5]. Calibration of the magnetic fields improves image quality but since there is no perfect magnetic field in real, bias field remains on the image.

Vlaardingerbroek and Boer et al. [6] mentioned bias field may lead false diagnosis. Expert physicians usually ignore visible bias field during examination, but physicians with less experience may perform false diagnosis. Furthermore visible and non-visible bias field is the major problem of image analysis, registration and segmentation (both manual and automated segmentation) techniques. For manual segmentation techniques, tissue boundary identification becomes more difficult for expert, who segments the tissues. Since bias field affects intensity values, automated segmentation techniques may fail, where they require a signal intensity model for different tissue types, especially for images with large bias field. Bias field also affects the performance of registration techniques, which may result unrealistic warps in nonlinear registration. Last, quantification analyses, which are image intensity based, may cause inaccurate results for the images, with significant bias field [5, 7, 8].

Since bias field or RF inhomogeneity is a major problem for both segmentation and registration, removal of this bias field is needed for better performance, and accurate results. In the last decades many studies have been proposed to eliminate this artifact.

Early methods for estimation and correction of inhomogeneity performed scanning of a test object or phantom to obtain the inhomogeneity field due to the coil [8, 9]. However these approaches assume that bias field is patient independent, which is not in real. Furthermore, it is required that the test object's scan parameters are the same as

the patient's, which makes these methods impractical. Also they require increased scan acquisition times [5, 7, 9].

Novel methods include post-processing techniques, and based on spatial inhomogeneity correction. Chen et al. [7] proposed a fuzzy c-means (FCM) based algorithm, which minimizes FCM objective function iteratively, that simultaneously estimates the bias field, while segmenting the brain MR image. Dawant et al. [10] proposed a least-square method based on spline fitting to bias field. Bias field is estimated as a linear combination of the spline functions with the weights, chosen to minimize the squared error of N reference points within one tissue class. Sled et al. [10] proposed the most commonly used bias field correction technique, N3, which is an automated technique, which sharpens the image histogram iteratively by deconvolving Gaussian fields from the subsequent estimates of the uncorrupted signal and spline smoothing the derived bias field. Vovk et al. [8] proposed a method that computes local estimation of intensity inhomogeneity from a two dimensional feature space in which intensity and spatial information are combined. Correction of bias field is obtained by spatial regularization of the local estimates. Leemput et al. [11] proposed a brain atlas method with assumption of a priori probability maps for each tissue class to automatically construct intensity models for each individual scan. Gerig et al. [12] made the assumption that pixels on the image belong to a certain tissue class, and pushes each pixel's intensity value to the very next preferred class mean.

Homomorphic filtering is also used generally since it is easy to implement. But as Tincher et al. [13], Fan et al. [14], and Guillemaud et al. [15] showed direct implementation of homomorphic filter results edge artifacts on the borders, and gives undesirable results since it uses information on the background and body pixels to estimate bias field, which they do not contain information related to bias field. Guillemaud et al. [15] proposed normalized convolution with homomorphic filtering technique to estimate the bias field that eliminates border artifacts between tissue and background, and undesirable effects. Brinkman et al. [16] applied modified mean-based homomorphic filtering with the assumption that image has certain tissue classes with certain intensity values for each class of tissue. She evaluates the effect of kernel size of the filter.

Information theoretical approaches also have been proposed that they use entropy minimization. Entropy was first proposed for image alignment by Viola et al. [17] and as an example he also used his method for bias correction, where bias field was constructed as polynomials. Bias field was estimated as the polynomial, which results the minimum uncorrupted image entropy. Likar et al. [18] also parameterized the shading according to brightness and contrast parameters and find the values that give the minimum entropy for the corrected image. Mangin et al. [19] proposed a cost function and search for the optimum correcting field, gives minimum entropy.

During last decades, as seen above, many methods were proposed for the correction of bias field. Although some methods proposed above give good results for especially brain MR images, there is little evidence that these methods work properly on breast MR images. MR imaging of the breast get more importance especially for breast cancer screening, and also diagnosis, there is still need a method for bias field correction that corrupt breast MR images.

Most of these methods require parameters to be specified such as tissue intensity values, or need templates or models to be fitted, or user control to such as specifying cutoff frequency of the homomorphic filter. Even non-parametric and user independent methods such as [5] only can correct specific bias fields (differential bias as in [5]). Above methods also suffer from assumption that each pixel's intensity belongs to a certain tissue class, which is usually not for breast tissue, and require user interaction to obtain best results, which is not objective.

For any proposed method from now on, should be fully automatic, user independent, non-parametric, and not model based. The main objective of this thesis is to develop a method which is fully automatic and non-parametric. Since main application objective of this thesis is breast MR images, and there are no certain tissue classes that can be specified for breast tissues (like in brain tissues, white matter, grey matter, CSF), and no model or template can be described for breast, we consider a method that does not rely on parametric or model based estimation. As we know that bias field is related to low-frequency components of the MR image, homomorphic filtering is a promising technique for our method, which does not require any parameters or models. Although Guillemaud et al. [15], and Brinkmann et al. [16]

suggested tissue segmentation to eliminate edge artifacts for homomorphic filtering. Main constraint of this method is that this method requires user control to define filter parameters. As we state above any method for bias field correction should be user independent we need to define a criterion to define filter parameter, for this thesis cutoff frequency, objectively. From information theoretical perspective as Viola et al. [17], Likar et al. [18] and Mangin et al. [19] showed, entropy can be used as an objective criterion to define filter parameter.

Our proposed method is based on Guillemaud's homomorphic filtering technique and its optimization with entropy minimization technique proposed by Mangin et al. [19], which is non-parametric and user independent. In this method we define a correcting field F_c and a function J of F_c which is a combination of uncorrupted image entropy and a measure of the field smoothness. Optimal correcting field F_c^{opt} minimizes $J(f_c)$ and results in the estimation of the optimum cutoff frequency of the homomorphic filter. Our method is simple, easy to implement, fast and effective. It does not require any parameters; such as tissue classes, and does not need user control (assignment of cutoff frequency).

3. METHOD

3.1 Introduction

RF inhomogeneity or bias field is defined as the changes in the field that caused slowly varying smooth intensity variation over the image. It affects image analysis, segmentation and registration techniques. Main reasons of this bias field are:

- Inhomogeneity of magnetic field, B_0;
- Inhomogeneity of the RF pulse generated by the oscillating secondary magnetic field, B_1;
- Nonuniformity of the receiver coils.

In general proposed methods for correction for RF inhomogeneity require parameters to be defined, and user control. In the present thesis work we propose a method that is non-parametric and user independent. It is based on Guillemaud's homomorphic filtering. Since this technique suffers from user control to specify cutoff frequency of the filter, we use an entropy minimization technique [19] to automatically estimate the cutoff frequencies.

Bias field, $B(x)$ causes a multiplicative corruption of MR images, and mathematically can be defined as follow:

$$I_{acquired}(x) = I_{uncorrupted}(x) \times B(x) + n(x) \tag{3.1}$$

where $I_{acquired}(x)$ is the acquired image intensity at voxel x; $I_{uncorrupted}(x)$ is the uncorrupted or ideal image intensity that tissue emits; $B(x)$ is the slowly varying smooth bias field and $n(x)$ is the image noise [20].

3.2 Homomorphic Filtering

In MR images, bias field is usually related to low frequency components, whereas the acquired image is related to high frequency components. By applying a high-pass filter to acquired image, we can remove the low-frequency components, and consequently remove the bias field. But since bias field is multiplicative, direct application of high-pass filter is impossible, because Fourier transform is not applicable to multiplicative forms.

When image is modeled as in Equation 3.1, homomorphic filtering can be used to separate two components, $I_{uncorrupted}(x)$ and $B(x)$ [21, 22]. However, we have to take the logarithm first and convert the multiplicative form to an additive form, before we can use Fourier transform and filtering.

Direct implementation of homomorphic filtering gives good results, when the inhomogeneity spreads all over the image. Since breast MR images have a uniform background, and inhomogeneity only spreads over the tissue region. Direct application of homomorphic filtering, results streak edge artifacts at the border, between tissue and background. For MR images, bias field could be estimated over the tissue region, where background contains no information about the bias [15]. Guillemaud et al. [15] showed that, removal of this incomplete or uncertain data from the image will eliminate edge artifacts at the border region.

In the present thesis work we first generate a "certainty image" to segment background and tissue region. To generate the certainty image, we use grey-level histogram thresholding, which is also known as Otsu's method. Since the bias field is related to low-frequency components of the image, we apply low-pass filtering to the thresholded image and estimate the bias field. The difference between the estimated bias field and the acquired image gives us the uncorrupted image.

3.2.1 Grey-level histogram thresholding

Thresholding is used to create a bilevel (monochrome, or black and white) image that should contain all of the essential information, which are the number, position and

shape of the objects [22]. The main idea behind grouping pixels by grey level is that pixels with similar levels in a neighborhood generally belong to the same object. Thus the complexity of the data can be reduced, this in turn, simplifies classification. The threshold should be determined from the pixel values of the image. The use of histograms is a common way of determining this threshold; it is defined as the lowest point between two peaks in the image histogram.

Otsu's method uses the idea that tissue and background pixels have different mean levels and different standard deviations and variances. We first compute the overall variance, σ_t^2, of the grey level values in the image. When there are two groups of pixels in the image for any given threshold, t, we also compute the variance of the tissue and the background pixels, that are within-class variance, σ_w^2. Next, we compute between-classes variance, σ_b^2, which is the variation of the mean values for each class from the overall mean of all pixels, μ_T. The optimum threshold t is defined as the value that minimizes the ratio of the between-class variance to total variance, which is:

$$\eta(t) = \frac{\sigma_b^2}{\sigma_t^2} \tag{3.2}$$

Equation 3.2 defines the needed ratio, and the value of t corresponding to the smallest value for η is the *best threshold*. Between-class variance is computed as:

$$\sigma_b^2 = \omega_0 \omega_1 (\mu_0 \mu_1)^2 \tag{3.3}$$

where,

$$\omega_0 = \sum_{i=0}^{t} p_i \ , \ \omega_1 = 1 - \omega_0 \tag{3.4}$$

$$\mu_0 = \frac{\mu_t}{\varpi_0} \ , \ \mu_1 = \frac{\mu_T - \mu_t}{1 - \varpi_0} \ , \ \mu_t = \sum_{i=0}^{t} i \cdot p_i \tag{3.5}$$

and p_i is the probability of grey level i. $\eta(t)$ is computed for all possible values of t, and the t that gives the smallest η is the optimal threshold.

We apply Otsu's method to the acquired image, $I_{acquired}(x)$ and obtain certainty image or tissue image, $I_{tissue}(x)$, which has the value 1 for tissue region (breast region), and 0 for background region. Figure 3.1 shows an acquired image and tissue image derived from it. After generating the tissue image, we take the logarithm of the acquired image and multiply it with tissue image to obtain:

$$I_{thresholded}(x) = Log\left[I_{acquired}(x)\right] \times I_{tissue}(x) \tag{3.6}$$

Both $I_{thresholded}(x)$ and $I_{tissue}(x)$ are low-pass filtered as described in the next section.

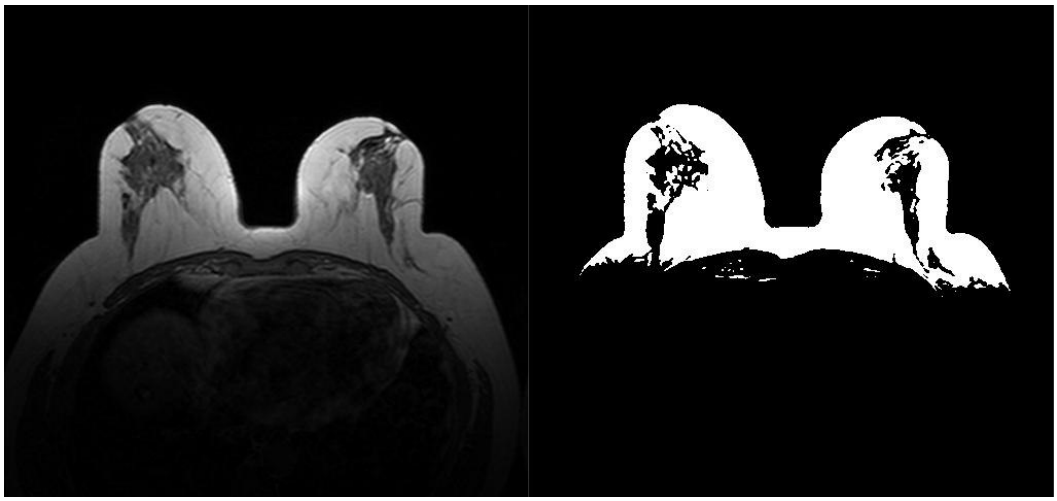

Figure 3.1 Example of tissue image, obtained from acquired images using Otsu's method.

3.2.2 Low-pass filtering

If we take the logarithm of (3.1), the multiplication operator is replaced by an addition operator and this makes it possible to apply low-pass filtering to the image. The low (bias field) and high frequency (uncorrupted image) components can than be separated as explained below:

$$Log\left[I_{acquired}(x)\right] = Log\left[I_{uncorrupted}(x)\right] + Log\left[B(x)\right] \tag{3.7}$$

We use a Butterworth low-pass filter for low-pass filtering. The transfer function of a Butterworth low-pass filter is given by:

$$H(u,v)=\frac{1}{1+\left[D(u,v)/D_0\right]^{2n}} \tag{3.8}$$

where n is the order of the filter, D_0 is the cutoff frequency, and $D(u,v)$ is the distance from point (u,v) to the origin of the frequency rectangle and is given by:

$$D(u,v)=\left[\left(u-M/2\right)^2+\left(v-N/2\right)^2\right]^{1/2} \tag{3.9}$$

Here, it is assumed that the image size is $M\times N$ [15]. Since it gave satisfactory results, the order of the low-pass filter is fixed to 4.

Before applying the low-pass filter, Fourier transforms of $I_{thresholded}(x)$ and $I_{tissue}(x)$ are determined from:

$$\mathcal{F}\left\{I_{thresholded}(x)\right\}=\mathcal{F}\left\{Log\left(I_{acquired}(x)\right)\times I_{tissue}(x)\right\} \tag{3.10}$$

$$=I_{thresholded}(u,v)$$

$$\mathcal{F}\left\{I_{tissue}(x)\right\}=I_{tissue}(u,v) \tag{3.11}$$

$$S_1(u,v)=H(u,v)\cdot I_{thresholded}(u,v) \tag{3.12}$$

$$S_2(u,v)=H(u,v)\cdot I_{tissue}(u,v) \tag{3.13}$$

where $S_1(u,v)$ is the low-pass filtered $I_{thresholded}(x)$ and $S_2(u,v)$ is low-pass filtered $I_{tissue}(x)$ in frequency domain. Our next step is to take the inverse Fourier transform of $S_1(u,v)$ and $S_2(u,v)$.

$$\mathcal{F}^{-1}\left\{S_1(u,v)\right\}=S_1(x)\ ,\ \mathcal{F}^{-1}\left\{S_2(u,v)\right\}=S_2(x) \tag{3.14}$$

3.2.3 Estimation of bias field and uncorrupted image

If we divide $S_1(x)$ to $S_2(x)$, we obtain the logarithm of the bias field, $Log(B(x))$:

$$Log\left(B(x)\right) = \frac{S_1(x)}{S_2(x)} \tag{3.15}$$

The logarithm of the uncorrupted image is obtained by subtracting $Log(B(x))$ from $Log\left(I_{acquired}(x)\right)$:

$$Log\left(I_{uncorrupted}(x)\right) = Log\left(I_{acquired}(x)\right) - Log\left(B(x)\right) \tag{3.16}$$

Taking the exponential of (3.16) we obtain $I_{uncorrupted}(x)$ as:

$$I_{uncorrupted}(x) = e^{Log\left(I_{uncorrupted}(x)\right)} \tag{3.17}$$

Due to the method used in the present thesis work, the resulting uncorrupted images have intensity values between 0 and 1. We should rescale the intensity level closer to the acquired image. This is easily performed by multiplying the uncorrupted image by the maximum intensity value of the acquired image.

Although the method described above gives good results, it needs user control to define the cutoff frequency of the low-pass filter. If the user specifies an inadequate low cutoff frequency, the bias field cannot be estimated properly. If the cutoff frequency is too high, the bias field would contain feature image information, which is not desired. To cope with this problem and make the method user independent, we estimate the optimum cutoff frequency using an entropy-based method. This is described in the next section.

3.3 Entropy Minimization

As Mangin et al. [19] stated, entropy can be used to measure image quality. If we had an ideal MR image, which has a certain intensity value for each tissue class, it would have low entropy. But since MR images suffer from bias field inhomogeneity,

which spread over tissue regions, and smoothly changes intensity values of the pixels, this intensity inhomogeneity causes higher entropy. Variation of the intensity values results in more grey levels; consequently more bins on the histogram, which leads to increase in entropy. An image corrupted by a bias field has a smooth histogram, where black and white regions are mixed. Removal of the bias field will decrease the intensity variations and grey levels will be collected to particular regions, which lead entropy to decrease. Uncorrupted images have histograms separated better than the corrupted images. Figure 3.2 shows histograms for acquired and uncorrupted images.

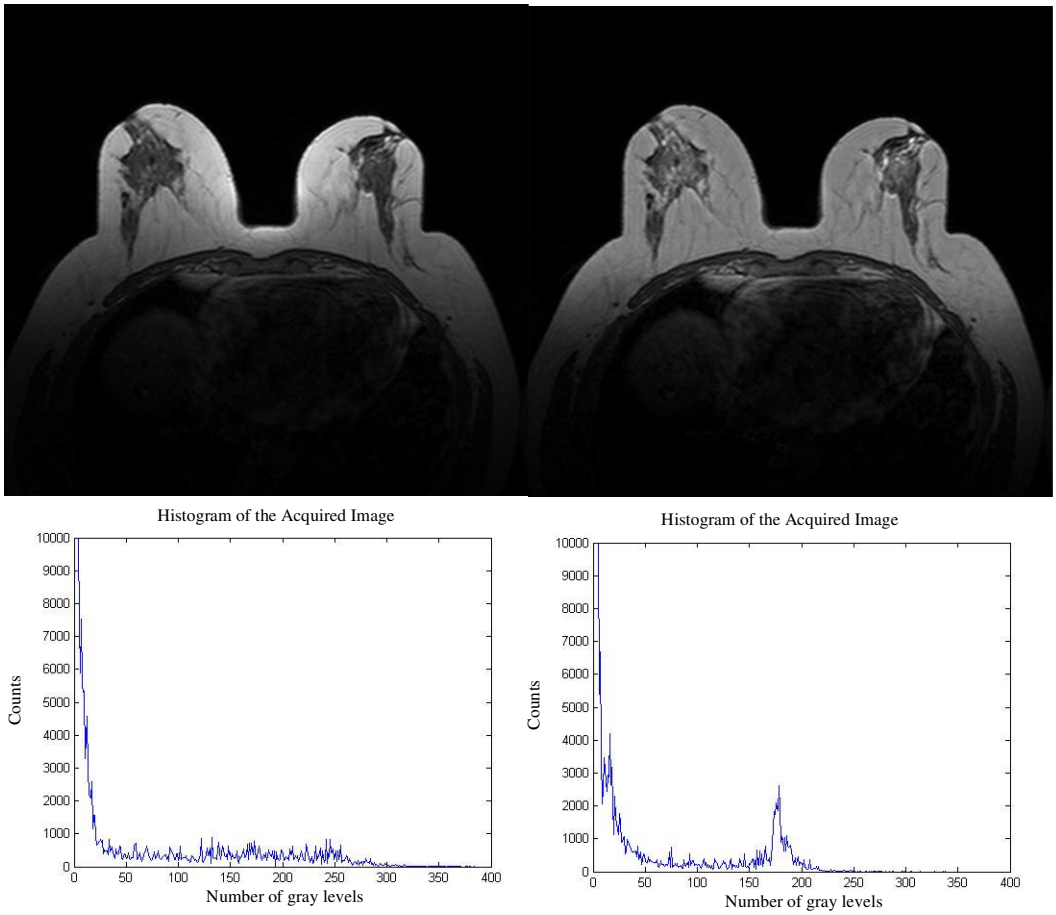

Figure 3.2 Example of histograms for the acquired and the uncorrupted images.

In Figure 3.2, the second row shows the corresponding histograms for acquired and uncorrupted images. Acquired image histogram is smoother, and has more grey level intensity values, which leads entropy to increase. However, uncorrupted image is

well separated for brighter and darker areas and grey level intensity values collected to particular regions (for this example around 200) leading entropy to decrease. For this example entropy of the acquired image is 3.6023 and entropy of the uncorrupted image is 3.4150.

From this perspective, we can define a function, $J(f_c)$, that combines bias field smoothness and image entropy. As mentioned above, since entropy is a good measure of image quality, $J(f_c)$ should include the entropy of the uncorrupted image. Also since the bias field should be smooth, a measure of the smoothness of the bias field should be included in $J(f_c)$. Moreover, since the optimum correcting field, F_c^{opt} minimizes $J(f_c)$ and results in a trade-off between field smoothness and image quality, a third term should be included into $J(f_c)$ to prevent this optimal field from being zero. To guarantee this the square of the difference of the mean values of the acquired and uncorrupted images is added.

The function used for correcting the bias field inhomogeneity, $J(f_c)$, and its relation to homomorphic filtering is discussed in the next section.

3.3.1 Cost function

We can define the cost function, $J(f_c)$ as follows:

$$J(F_c) = K_S \cdot S\left(I_{uncorrupted}(x)\right) + K_R \cdot R\left(B(x)\right) + K_M \cdot M(x) \tag{3.18}$$

where $S\left(I_{uncorrupted}(x)\right)$ is the uncorrupted image entropy, $R(B(x))$is the smoothness measure of the estimated bias field, and $M(x)$ is the square of the difference of the mean values of acquired image and uncorrupted image. K_S, K_R and K_M are positive constant weights, that are specified empirically.

The concept of entropy (in information systems) was first introduced by Shannon, and is defined as:

$$H(I) = -\sum_{i=1}^{n} p(I_i)\log(p(I_i)) \tag{3.19}$$

where n is the total number of possible symbols (grey level values of the pixels), and $p(I_i)$ is the probability of the i^{th} grey level value, that it may occur. According to above definition we compute $S(I_{uncorrupted}(x))$ as follow:

$$S(I_{uncorrupted}(x)) = -\sum_{i} \frac{H_{I_{uncorrupted}}(i)}{n_v} \cdot \log\left(\frac{H_{I_{uncorrupted}}(i)}{n_v}\right) \tag{3.20}$$

where n_v is the total number of pixels, and $H_{I_{uncorrupted}}(i)$ is the number of locations with intensity value, i, which can be calculated from the histogram of true image. A graph of the computed entropy of uncorrupted images for each cutoff frequency is shown in Figure 3.3.

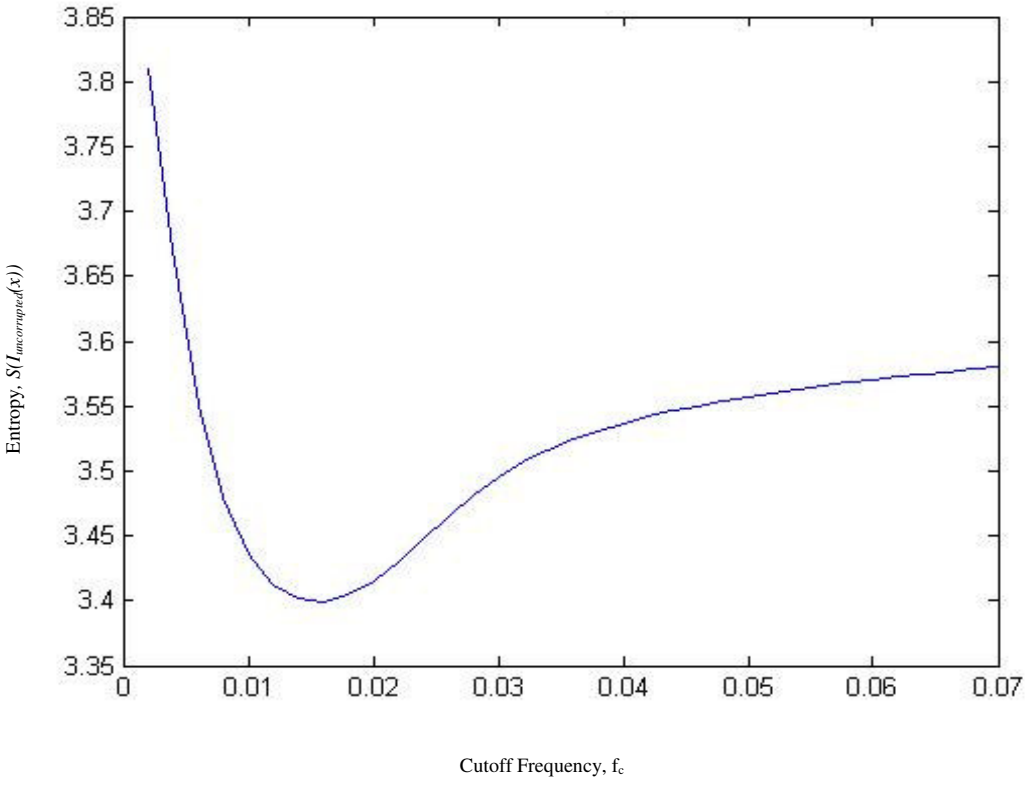

Figure 3.3 Graph of the computed entropy of uncorrupted images', $S(I_{uncorrupted}(x))$, for each cutoff frequency.

Smoothness of a field can be achieved via various methods. As any field gets smoother, the intensity difference between the neighbor pixels will decrease. Therefore, to measure the smoothness of the bias field, for each pixel, we take the difference of the intensity values between its neighbor pixels and take their square. Finally we sum the squared differences of all pixels and calculate the total smoothness of the bias field. $R(B(x))$ is defined as follow:

$$R(B(x)) = \sum_i B(i) \tag{3.21}$$

where $B(i)$ is the sum of the squares of intensity value differences of the pixels which are neighbor to the i^{th} pixel.

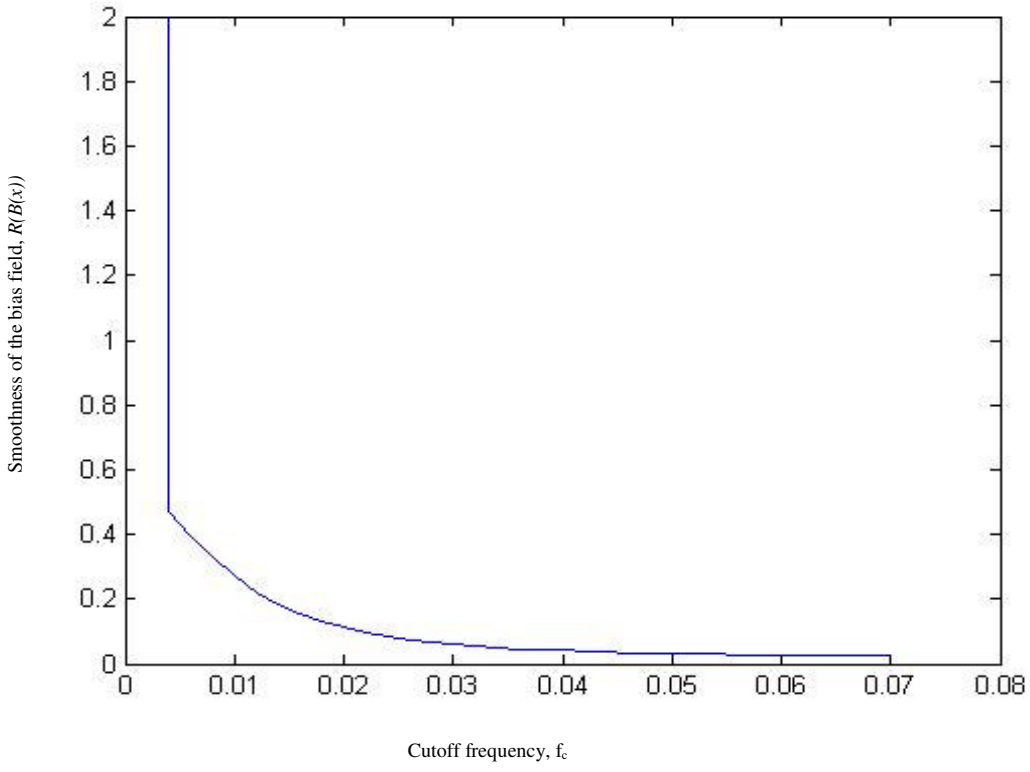

Figure 3.4 Graph of the smoothness of bias field, $R(B(x))$ for each cutoff frequency

For relative to constant fields, global minimum of the $J(f_c)$ would be a null field, since smoothness measure become minimal and entropy decreases consistently. $M(x)$ is added as a third term, to prevent $J(f_c)$ being null, and defined as:

$$M(x) = \left(\mu_{I_{uncorrupted}} - \mu_{I_{acquired}}\right)^2 \tag{3.22}$$

where $\mu_{I_{uncorrupted}}$ is the mean value of uncorrupted image and $\mu_{I_{acquired}}$ is the mean value of acquired image.

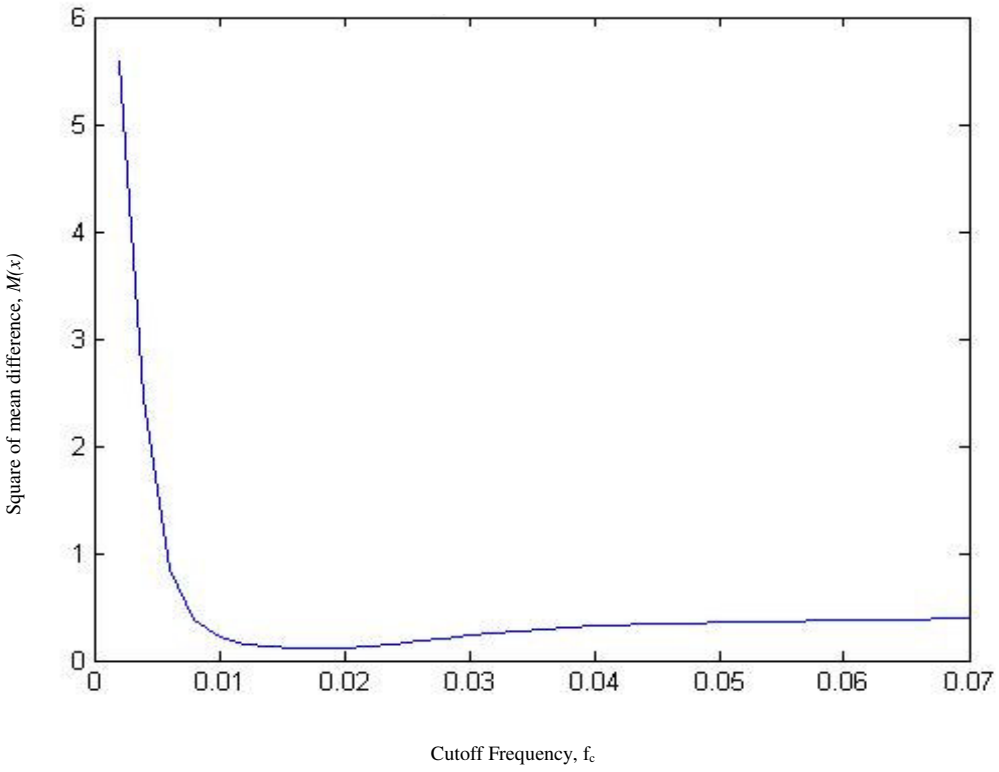

Figure 3.5 Graph of the square of mean difference, $M(x)$ for each cutoff frequency

K_S, K_R and K_M are balancing constant weights. Since the entropy of the uncorrupted image has an amplitude up to ten, and the smoothness and the mean difference has amplitude up to hundreds, these weights should be specified to make the amplitude ranges equal. Since the mean difference is the term used to prevent the correcting field to be a null field, K_M should be chosen low, in order to prevent $M(x)$ to affect the shape of $J(f_c)$. With the above considerations, the value of K_S is fixed to 1; K_R is fixed to 0.00125 and K_M is fixed to 0.005. Figure 3.3-3.6 show graphs of $S(I_{uncorrupted}(x))$, $R(B(x))$, $M(x)$ and $J(f_c)$.

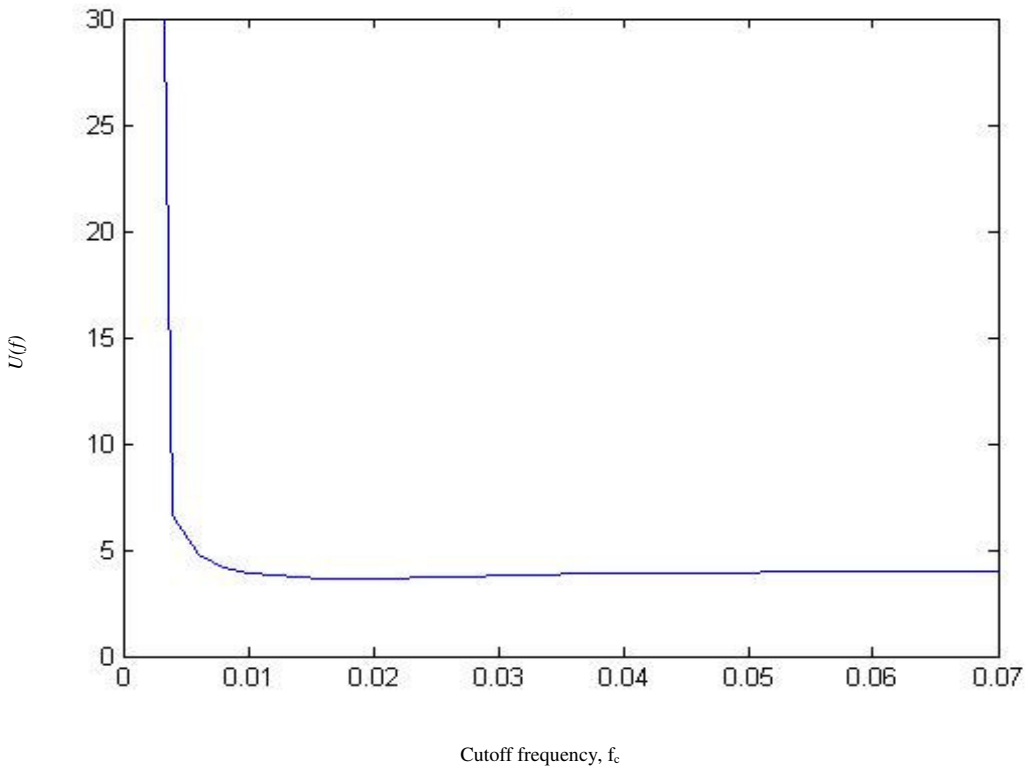

Figure 3.6 Computed $J(f_c)$, which is sum of $S(I_{uncorrupted}(x))$, $M(x)$ and $R(B(x))$ for each cutoff frequency

3.3.2 Optimization

In order to implement entropy minimization to homomorphic filtering, we first define a cutoff frequency range. For each cutoff frequency we derive an estimated bias field and an uncorrupted image by homomorphic filtering. Then, from the estimated bias field and the uncorrupted image we compute $J(f_c)$ for each cutoff frequency. The optimum cutoff frequency of the homomorphic filter is the value which gives the global minimum of $J(f_c)$, hence the resulting optimum correcting field, F_c^{opt}.

3.3.3 Search for global minimum

To find out the global minimum of $J(f_c)$ and the estimate F_c^{opt}, we simply use a gradient technique. We take the first derivative of the $J(f_c)$ and search for the cutoff frequencies, f_c, that make it equal to zero.

$$\frac{dJ(F_c)}{df_c} = 0$$

gives the extrema (minima and maxima). If there is any cutoff frequency that make $J'(F_c) = 0$, then we take the second derivative of $J(f_c)$, and search for the cutoff frequencies that make second derivative of the $J(f_c)$ greater than zero.

If there is more than one cutoff frequency that make $J''(F_c) > 0$, then we look for the $J(f_c)$ values for estimated cutoff frequencies. The minimum of these values gives us the optimum cutoff frequency.

3.3.4 Summary

Our method starts by estimating a threshold value by Otsu's method for a given breast MR image. From this estimated threshold, we create a tissue image. Then we take the logarithm of the given image, and multiply it with tissue image element by element. We apply low pass filtering with the first cutoff frequency in the specified range to the resulting image and the tissue image. We then estimate the bias image simply by

dividing these low pass filtered images. The difference of the estimated bias and the logarithm of the acquired image will give us the uncorrupted image. Next we compute the entropy of the uncorrupted image, smoothness of the bias field and the mean differences of the uncorrupted image and the acquired image. Computed entropy, smoothness and mean differences multiplied by the weights and the sum of these gives the value of $J(f_c)$ for this cutoff frequency. Then the cutoff frequency is increased, and above computations repeated. When this process ends for the given range of cutoff frequencies, we can estimate the global minimum of the $J(f_c)$ function. The cutoff frequency that makes $J(f_c)$ globally minimum is our optimum cutoff frequency. Using this, we estimate the uncorrupted image and bias field for this optimum value. A flowchart of proposed method is given in Figure 3.7.

3.4 Performance Evaluation

In order to evaluate our results, a quantitative assessment should be defined. Since entropy is related to information on the image, it can be used as a quantitative assessment. The difference of the entropies between the uncorrupted and the acquired images gives the information lost during processing. However, the effect of the bias field varies locally and as a result the performance of the proposed method varies on different regions of the image. Furthermore, background and patient's body should not be included, since they do not contain information about bias field. A surface is applied to acquired and uncorrupted images, and breast region is segmented from background and patient's body. This surface data is supplied by Gökhan ERTAŞ. In order to measure the performance locally, we segment the image into blocks and compute each blocks' entropy. Average information loss can be acquired as follow:

$$E = \frac{1}{n}\sum_{i=1}^{n}\left(S_{acquired}(i) - S_{uncorrupted}(i)\right)^2 \tag{4.1}$$

$$n = \frac{M \times N}{m \times m}$$

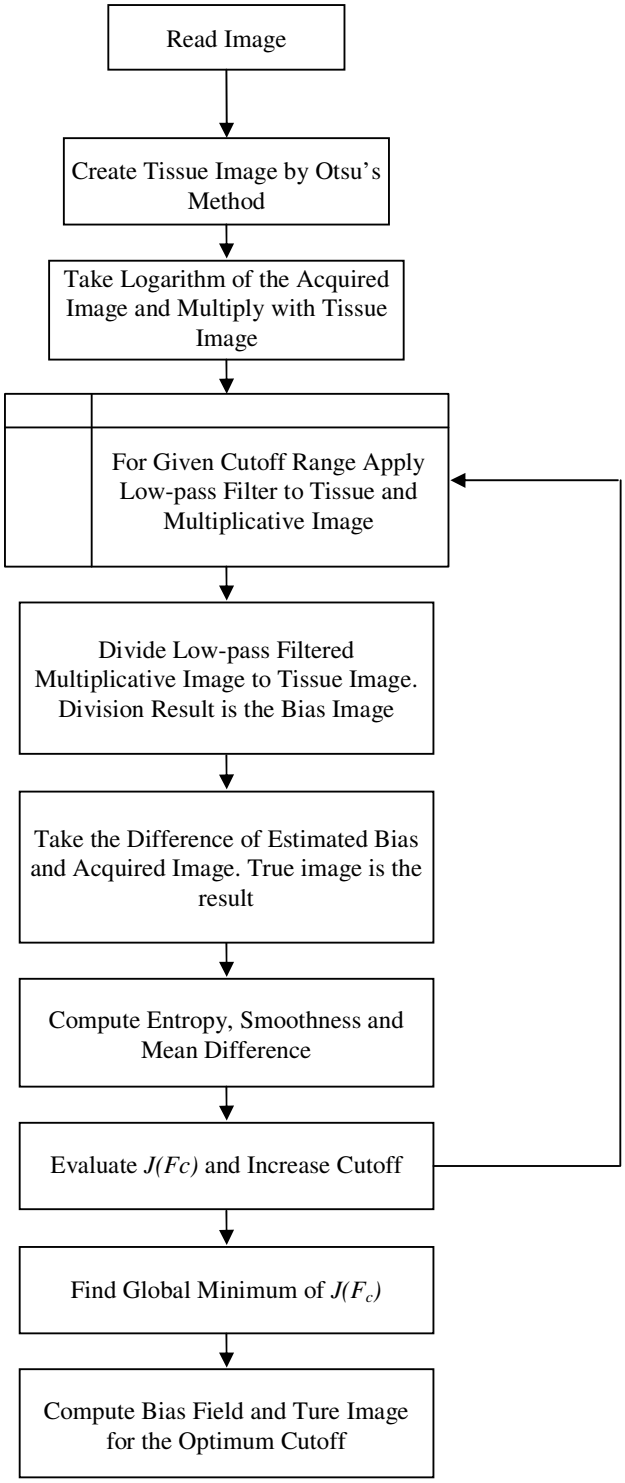

Figure 3.7 Flowchart of the proposed method.

where, $M \times N$ is the size of image (512 x 512 for our image set), $m \times m$ is the size of each block (16 x 16 for our evaluation) and $S_{acquired}(i)$ and $S_{uncorrupted}(i)$ are entropies of i^{th} block. The results are summarized in Table 3.1.

Table 3.1
Estimated cutoff frequencies, and related average information loss for images. Average *E* is 0.0041. N.E. is Not Estimated.

Patient	Diagnosis	Image Number	Estimated Cutoff	E	Patient	Diagnosis	Image Number	Estimated Cutoff	E
Patient 1, Age 40	Fibrocystic changes, Benign	Slice 6	0,0160	0,0058	Patient 6, Age 28	Sclerosis adenoma, Benign	Slice 6	N.E.	
		Slice 12	0,0160	0,0048			Slice 12	N.E.	
		Slice 22	0,0200	0,0056			Slice 22	N.E.	
		Slice 32	0,0400	0,0028			Slice 32	N.E.	
		Slice 38	N.E.				Slice 38	N.E.	
Patient 2, Age 49	Healthy	Slice 6	0,0160	0,0045	Patient 7, Age 45	Invasive ductal carcinoma, Malignant	Slice 6	0,0400	0,0021
		Slice 12	0,0300	0,0039			Slice 12	0,0460	0,0020
		Slice 22	0,0280	0,0037			Slice 22	0,0200	0,0046
		Slice 32	0,0480	0,0023			Slice 32	N.E.	
		Slice 38	0,0180	0,0053			Slice 38	N.E.	
Patient 3, Age 51	Invasive ductal carcinoma, Malignant	Slice 6	N.E.		Patient 8, Age 34	Healthy	Slice 6	0,0300	0,0024
		Slice 12	0,0280	0,0051			Slice 12	N.E.	
		Slice 22	0,0200	0,0051			Slice 22	N.E.	
		Slice 32	0,0500	0,0035			Slice 32	0,0320	0,0016
		Slice 38	0,0600	0,0034			Slice 38	0,0500	0,0014
Patient 4, Age 52	Invasive lobular carcinoma, Malignant	Slice 6	0,0140	0,0070	Patient 9, Age 32	Invasive papillary carcinoma, Malignant	Slice 6	0,0600	0,0023
		Slice 12	0,0160	0,0065			Slice 12	0,0420	0,0036
		Slice 22	0,0100	0,0071			Slice 22	0,0260	0,0048
		Slice 32	0,0120	0,0063			Slice 32	0,0280	0,0029
		Slice 38	0,0620	0,0032			Slice 38	N.E.	
Patient 5, Age 53	Fibro adenoma, Benign	Slice 6	0,0500	0,0044	Patient 10, Age 77	Healthy	Slice 6	0,0520	0,0028
		Slice 12	0,0620	0,0046			Slice 12	0,0540	0,0044
		Slice 22	0,0200	0,0058			Slice 22	0,0220	0,0041
		Slice 32	N.E.				Slice 32	N.E.	
		Slice 38	N.E.				Slice 38	0,0300	0,0055

4. RESULTS

4.1 Application Details

Matlab language is used to develop the necessary codes. The images are acquired using a 1.5 T Siemens MR and were supplied to us as a courtesy of İstanbul University, İstanbul Medical Faculty. They are precontrast T1 weighted images in DICOM format, obtained using 3D Flash sequences (TR/TE 11.7/4.2 ms, flip angle 25, field of view 320*320 mm, matrix size 512*512, slice thickness 2.5 mm, 0.625*0.625 mm resolution in x and y directions). The order of the Butterworth low-pass filter used is 4. K_S is fixed to 1, K_R is fixed to 0.00125 and K_M is fixed to 0.005. The cutoff frequency range is between 0.002 and 0.07, with the increment of 0.002, which results 35 iterations for each image.

To evaluate the effectiveness of the proposed method 50 breast MR images, from 10 different patients are processed. 3 of the patients are healthy individuals, 3 of them have benign findings and 4 of them have malignant findings.

As stated above, properties of the breast tissue varies from patient to patient. Furthermore even for the same patient, tissue properties changes by time. Consequently to demonstrate the proposed method a variety of images, having different tissue characteristics are used.

Estimated cutoff frequencies and average information loss are shown in Table 3.1, presented in page 30. Independent from the breast type, cutoff frequencies are estimated for 35 images of the given set. Related $J(f_c)$ functions have at least one or more minima. For healthy individuals the average of the $J(f_c)$ is 0.034, for patients having malignant findings it is 0.033 and for patients having benign findings average of it is 0.032.

Except for one patient (Patient 6), when there is no minima of the $J(f_c)$, there is a region where the slope of the function decrease and the correcting function tends to

become relatively flat; it does not continuously go towards a minimum. The results show that the cutoff frequencies at these relatively flat regions are also "optimal". Since we look for the minimum of $J(f_c)$, no estimation can be made using the method discussed in this work.

4.2 Evaluation

For quantitative evaluation, the average information loss, *E* is computed for each image. For higher cutoff frequencies, uncorrupted images contain more frequency components, both low and high. Thus, as the cutoff frequency increases, the difference between the acquired and the uncorrupted images decrease and as a consequence *E* decreases. The mean value of *E* is 0.00415; this value is too low with respect to the information the acquired images contain. This illustrates that our method mostly preserves the information on the images, which is very important for both visual interpretation and image analysis or diagnostic systems. Even for images severely affected by bias field inhomogeneity, it is 0.0071 at the most.

We can demonstrate our results in three groups; the first group has less fibrous tissue, the second group has equal allocation of both fibrous tissue and fat, and the last group has less fat but more fibrous tissue. We first give some typical examples of these groups and other examples are also given later.

The first example in Figure 4.1a belongs to a healthy individual (Patient 10, Slice 22), who has a fatty breast tissue, which contains little fibrous mass. The image on the left is the acquired image, that in the middle is the uncorrupted image and that on the right is the image due to the bias field inhomogeneity. Related mesh surfaces are shown in the second row. The graph of the correcting function, $J(f_c)$ is given in Figure 4.1b. For this example $J(f_c)$ has a global minimum at 0.022. As it can be seen from the figure, our method largely removes the bias field but preserves the inner structure of the breast. Moreover, the chest wall and the breast structures around it become more visible; uncorrupted image has no edge artifact on the border of background and the breast tissue. Mesh surfaces illustrate how intensity values become closer and their variation become less than that of the acquired image.

The next three figures, Figures 4.2b, 4.3a and 4.4b are examples of breast tissues with almost equal amount of fibrous and fatty tissue. Figure 4.2b belongs to a patient (Patient 1, Slice 22) with benign findings, Figure 4.3a belongs to a healthy individual (Patient 8, Slice 32) and Figure 4.4b belongs to a patient (Patient 3, Slice 22) with malignant findings. Figures 4.3a and 4.4b are severely corrupted by the bias field, but it is removed properly, and has no visual effect. Furthermore dense and soft tissues become more discriminable, despite their less intensity variations. Also the chest wall and the breast tissue close to the body become more visible. However in Figure 4.2b and Figure 4.4b edge artifacts (bright regions), occur in and around fibrous tissue, which is an undesired effect of the homomorphic filter and can be seen on the mesh surfaces as peaks in the breast region. This results from the non-proper segmentation of the acquired image. Although Figure 4.3a contains largely fibrous tissue, better segmentation of the acquired image prevents edge artifacts. Also in the uncorrupted images, inner structures are preserved. For Figure 4.2b the estimated cutoff is 0.02, for Figure 4.3a it is 0.032 and for Figure 4.4b it is 0.02. Graphs of the related $J(f_c)$ functions are given in the Figure 4.2a,

Figure 4.5a is an example of dense breast tissue, with a sharp bias field, which belongs to Patient 6 (Slice 22) with the benign findings. The bias field is restricted to the breast edges and has no smooth variation over the image. The structure of the bias field causes $J(f_c)$ to decrease continuously, without having a minimum. However, around 0.01, the slope of the function decreases and it becomes relatively flat, which can be estimated as the optimum cutoff frequency. It cannot be detected due to search algorithm. However the inner structure in the uncorrupted image becomes more visible and intensity variations decrease even for high cutoff frequencies. In fact, for low frequencies, it is the bias field is mostly removed. For this example, uncorrupted image and bias field is estimated for the cutoff frequency of 0.07. The graph of the related $J(f_c)$ function is presented in the Figure 4.5b.

Appendix A includes other examples and gives brief explanations.

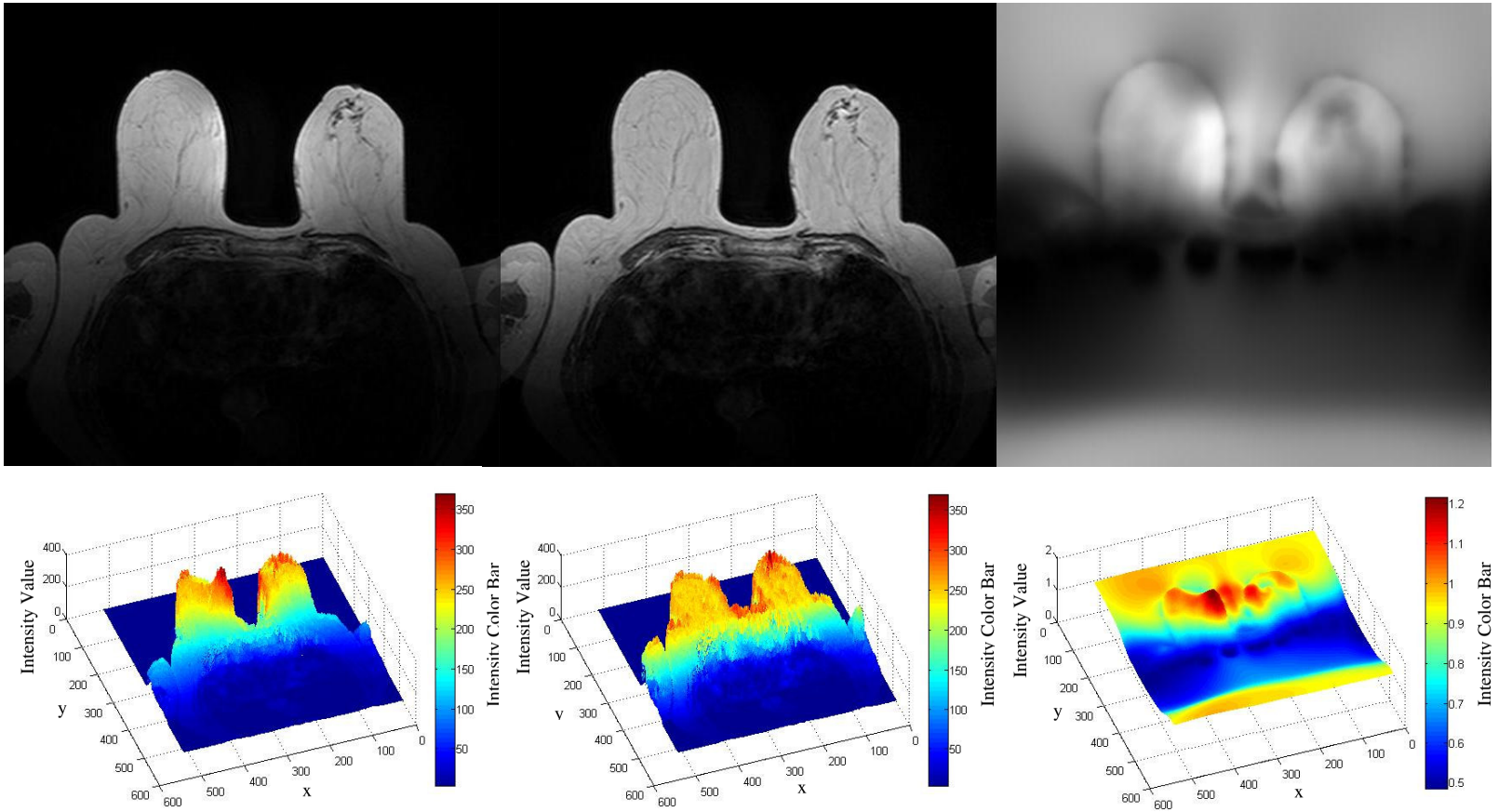

Figure 4.1a Estimated cutoff = 0.022, average information loss, E = 0.0041

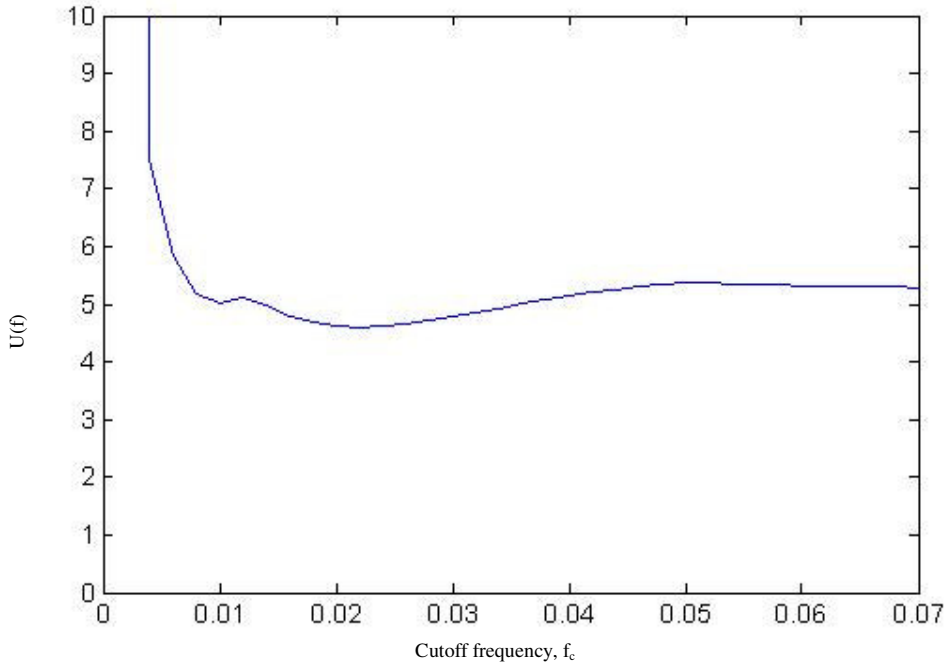

Figure 4.1b Computed $J(f_c)$ function of Figure 4.1a

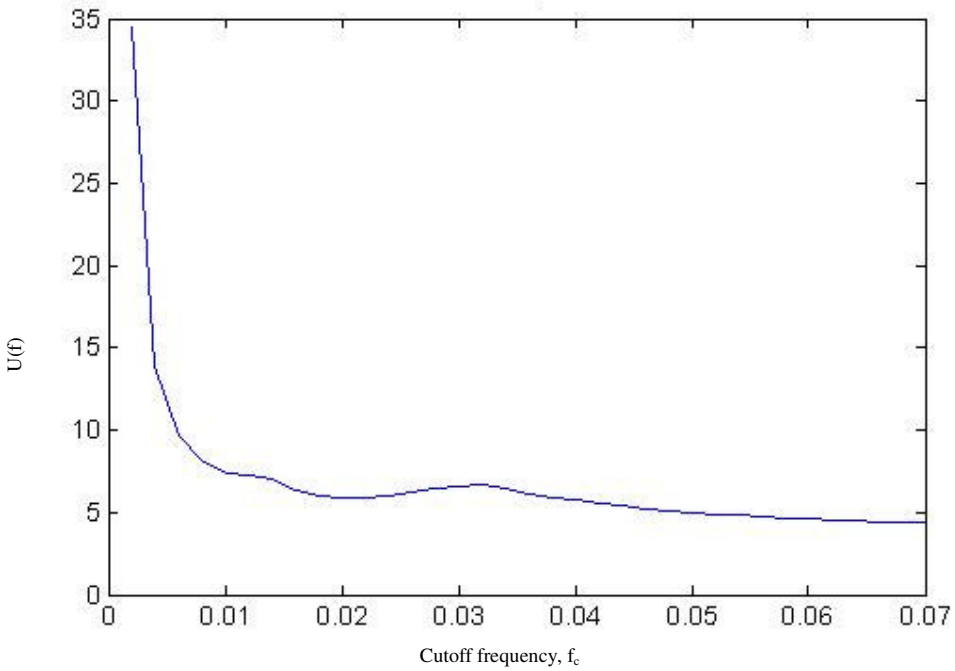

Figure 4.2a Computed $J(f_c)$ function of Figure 4.2b

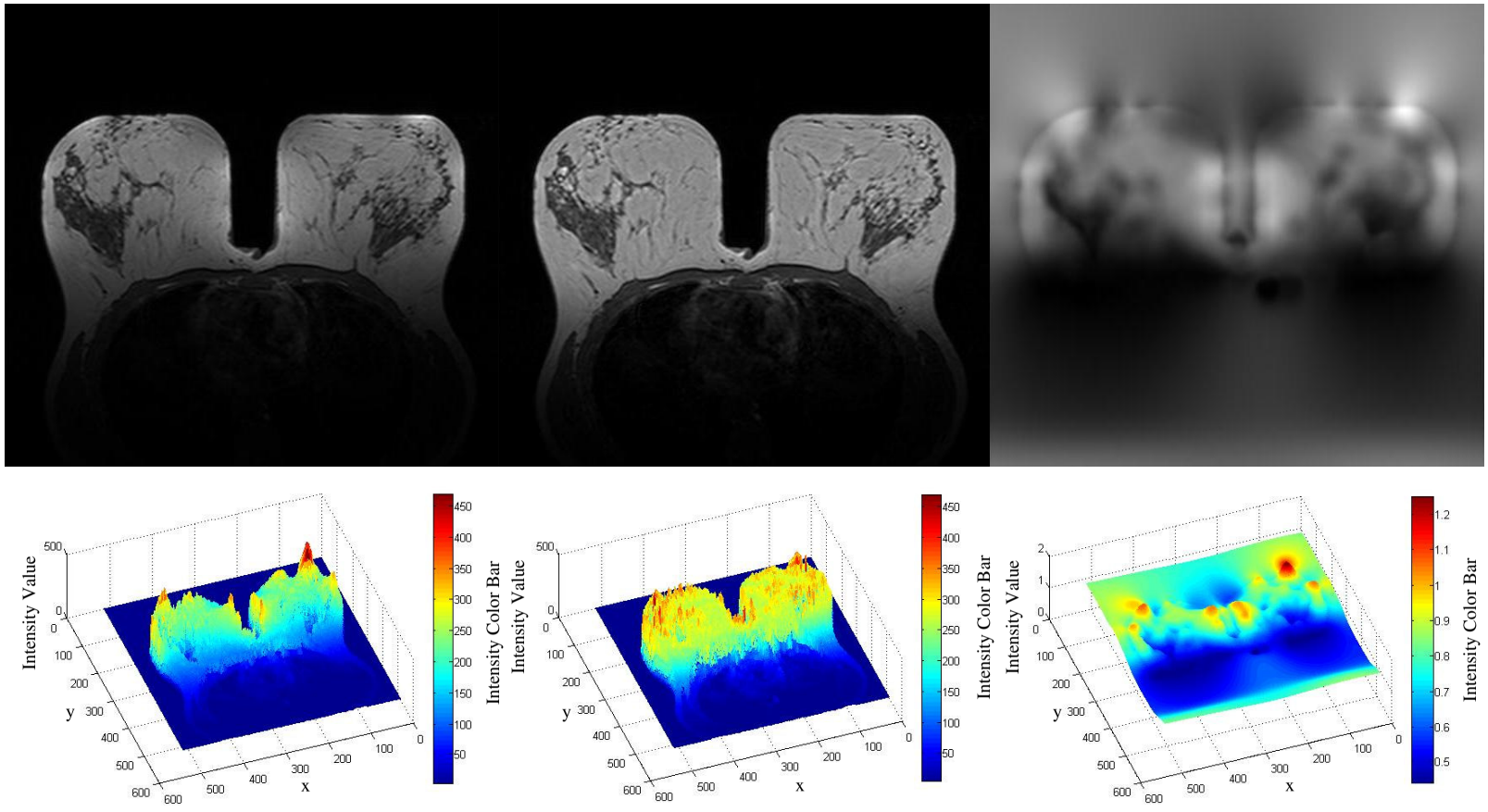

Figure 4.2b Estimated cutoff = 0.020, average information loss, E = 0.0056

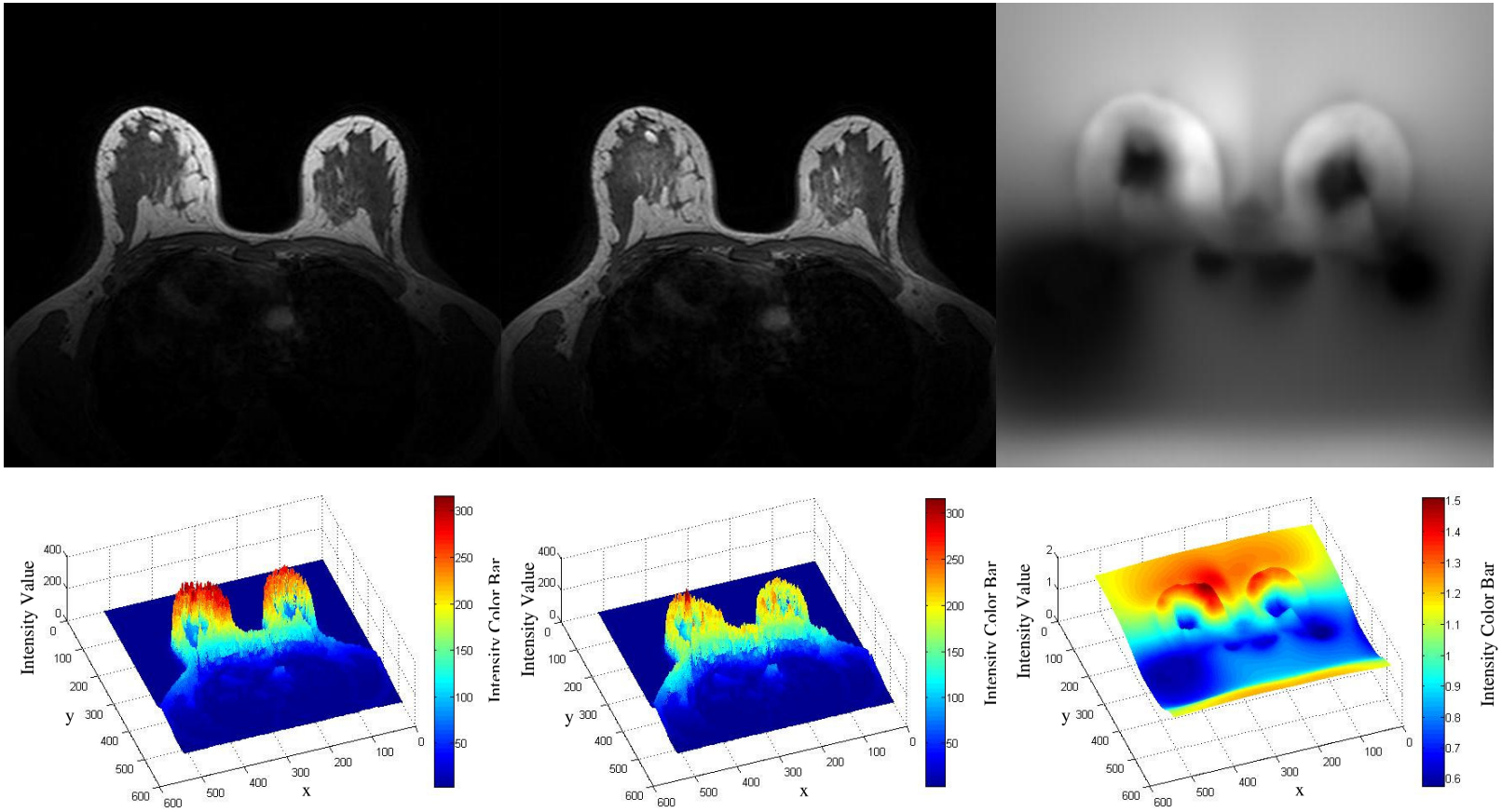

Figure 4.3a Estimated cutoff = 0.030, average information loss, E = 0.0016

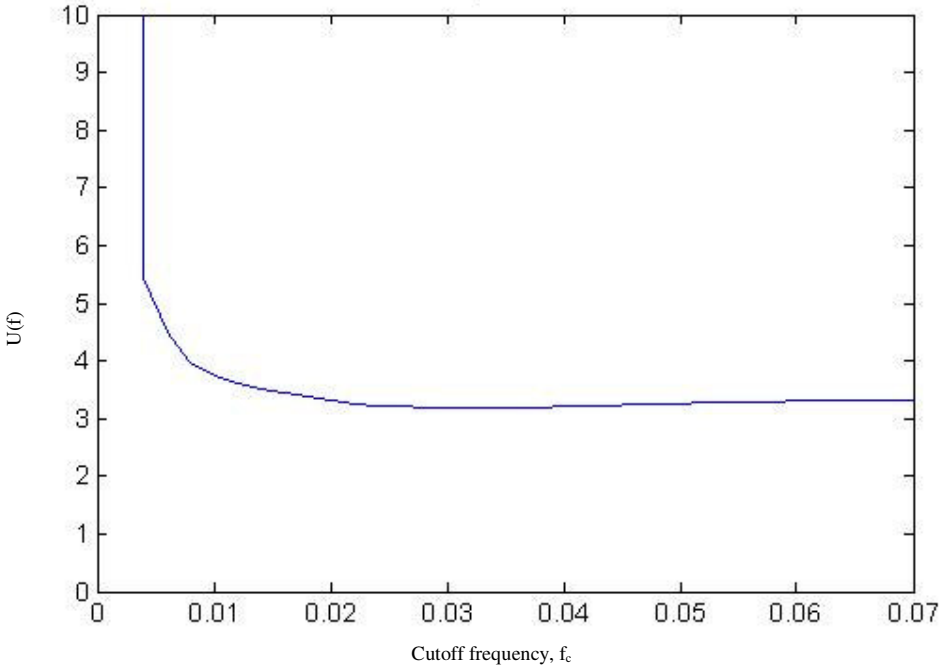

Figure 4.3b Computed $J(f_c)$ function of Figure 4.3a

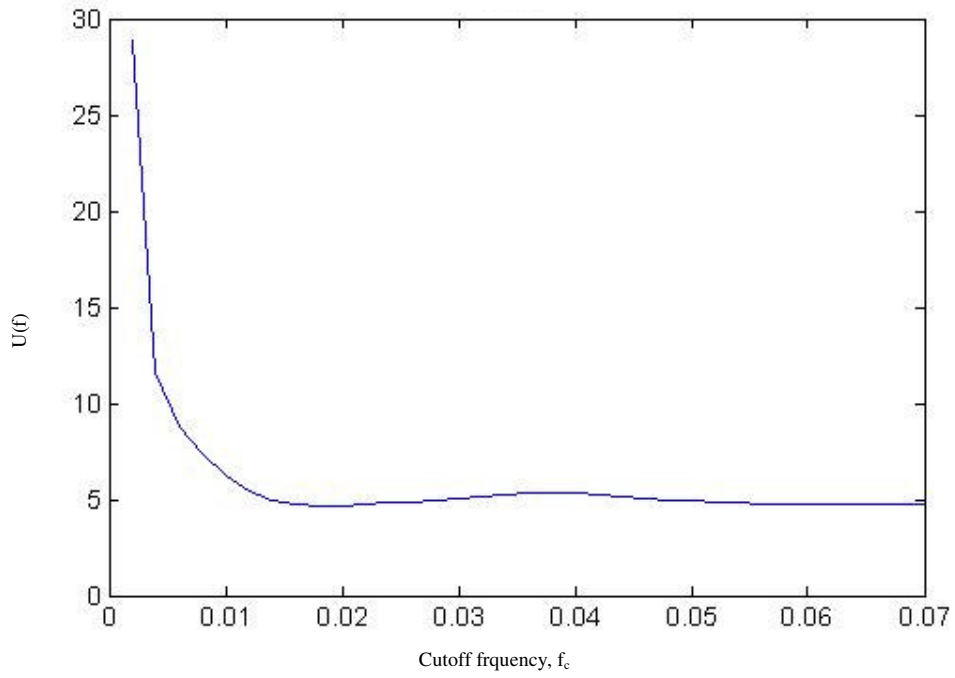

Figure 4.4a Computed $J(f_c)$ function of Figure 4.4b

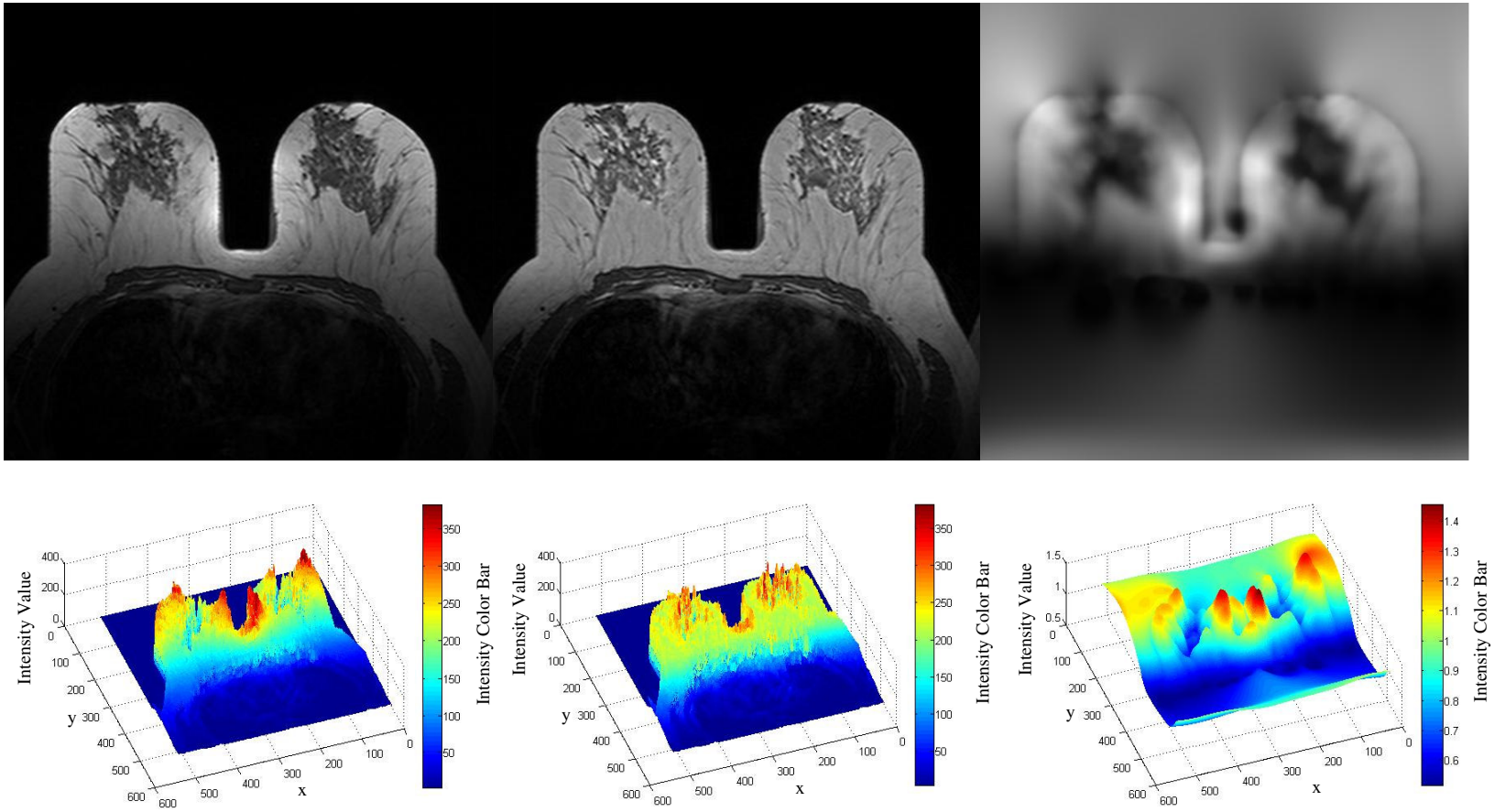

Figure 4.4b Estimated cutoff = 0.020, average information loss, E = 0.0051

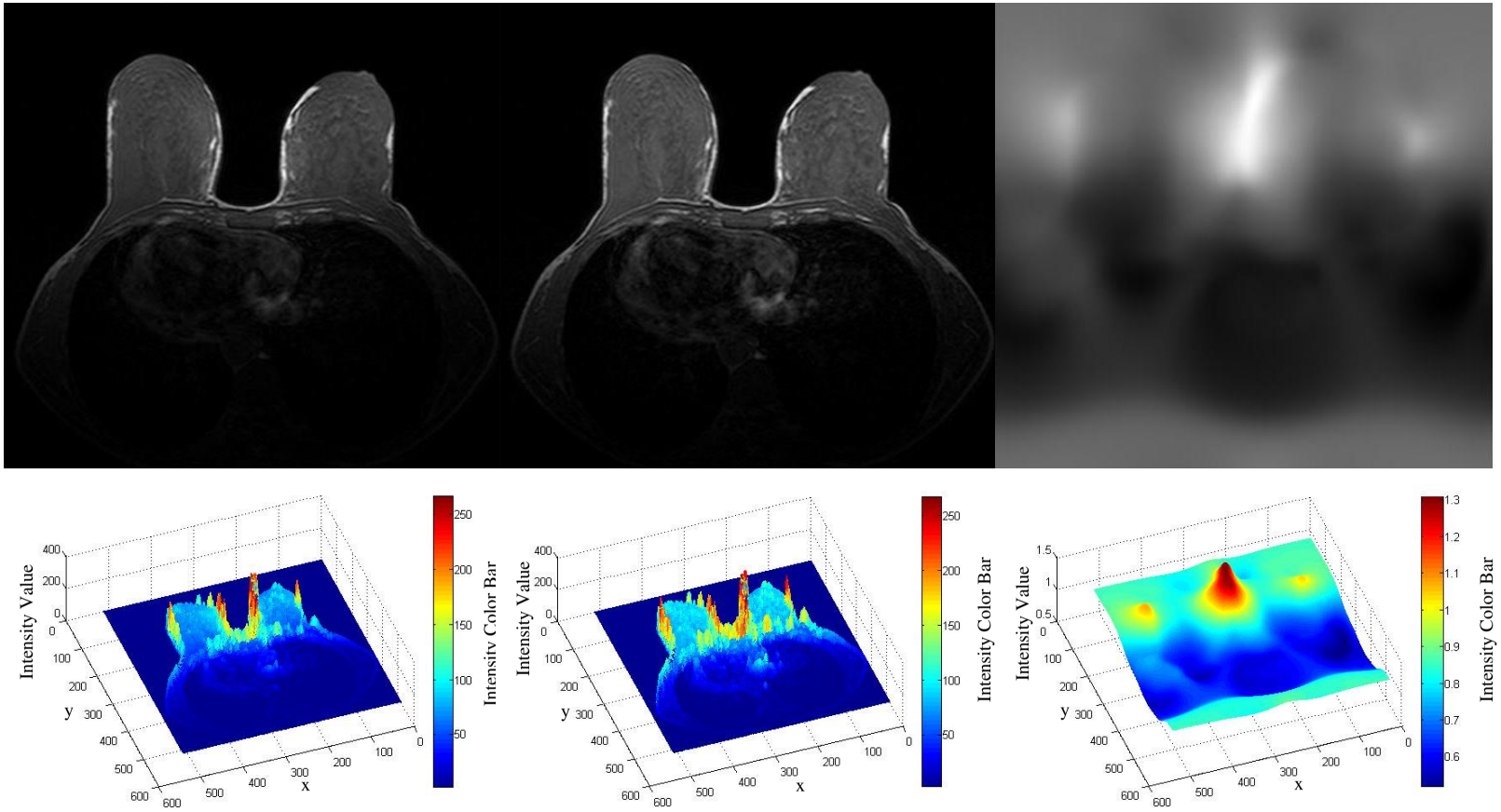

Figure 4.5a No estimated cutoff

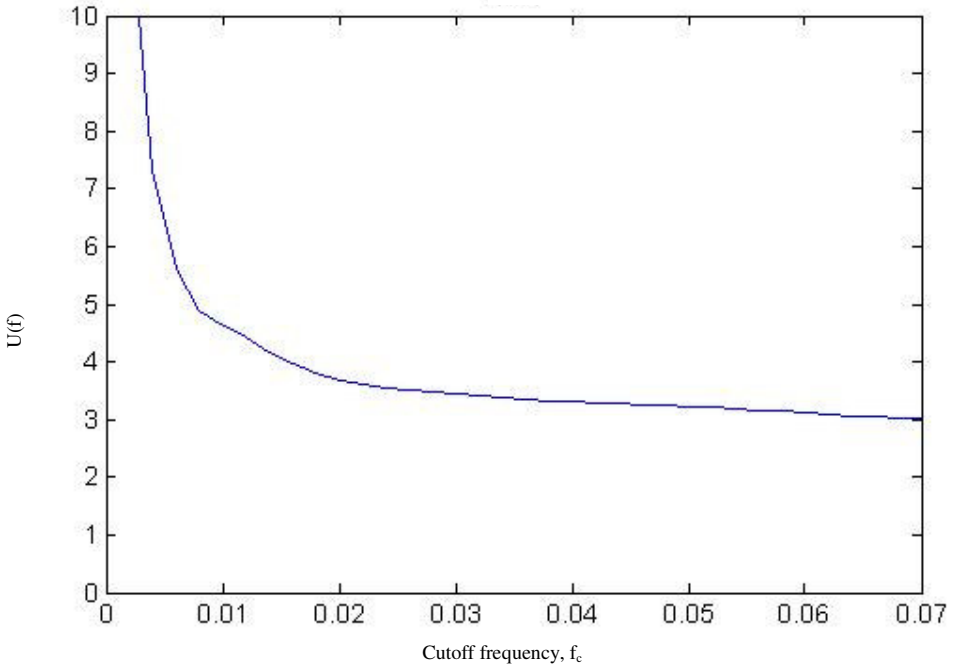

Figure 4.5b Computed $J(f_c)$ function of Figure 4.5a. No estimated cutoff

Figure 4.8 and 4.9 illustrates the effect of cutoff frequency. The images processed using cutoff frequencies below the optimum contain (bias field inhomogeneity related) "superfluous" information. As a result images loose some details, and the inner structures are not preserved properly. On the other hand, using frequencies higher than the optimum cutoff frequency the bias field cannot be estimated adequately and artifacts cannot be minimized properly. Figure 4.8 belongs to a healthy individual (Patient 2, Slice 22) and Figure 4.9 belongs to a patient (Patient 5, Slice 22) with benign findings. Acquired images are given in the Figure 4.6 and 4.7 respectively.

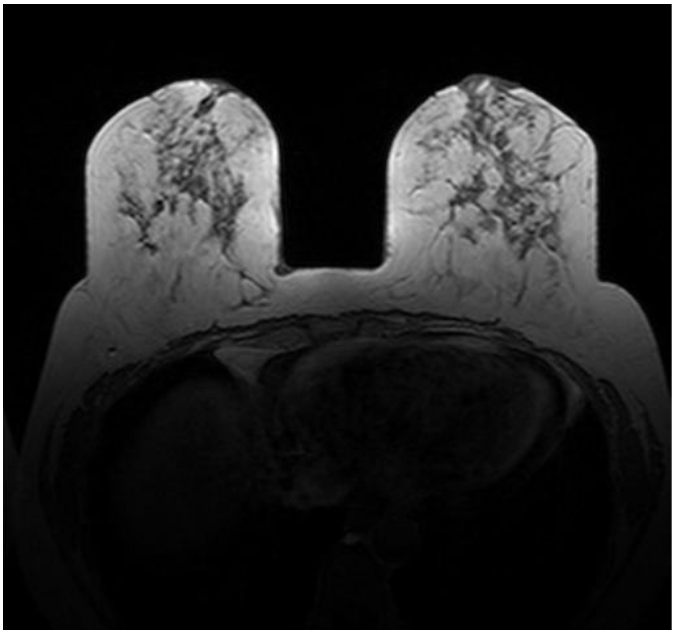

Figure 4.6 Acquired image of patient 2

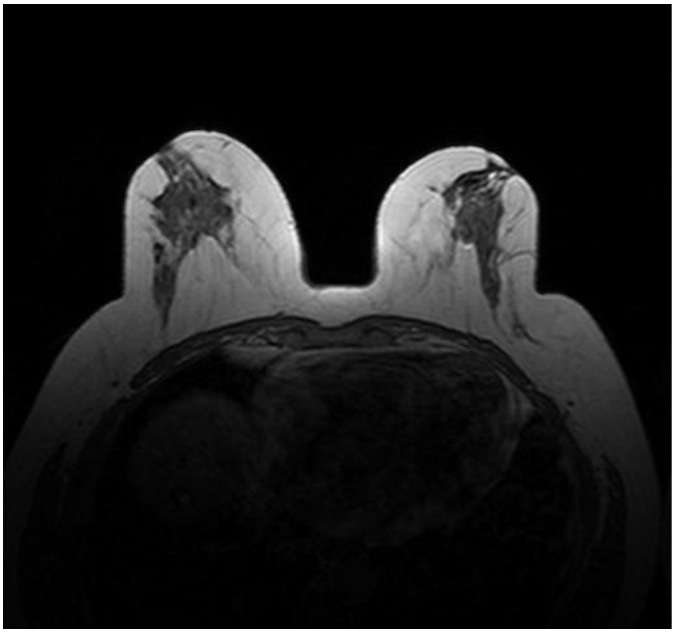

Figure 4.7 Acquired image of patient 5

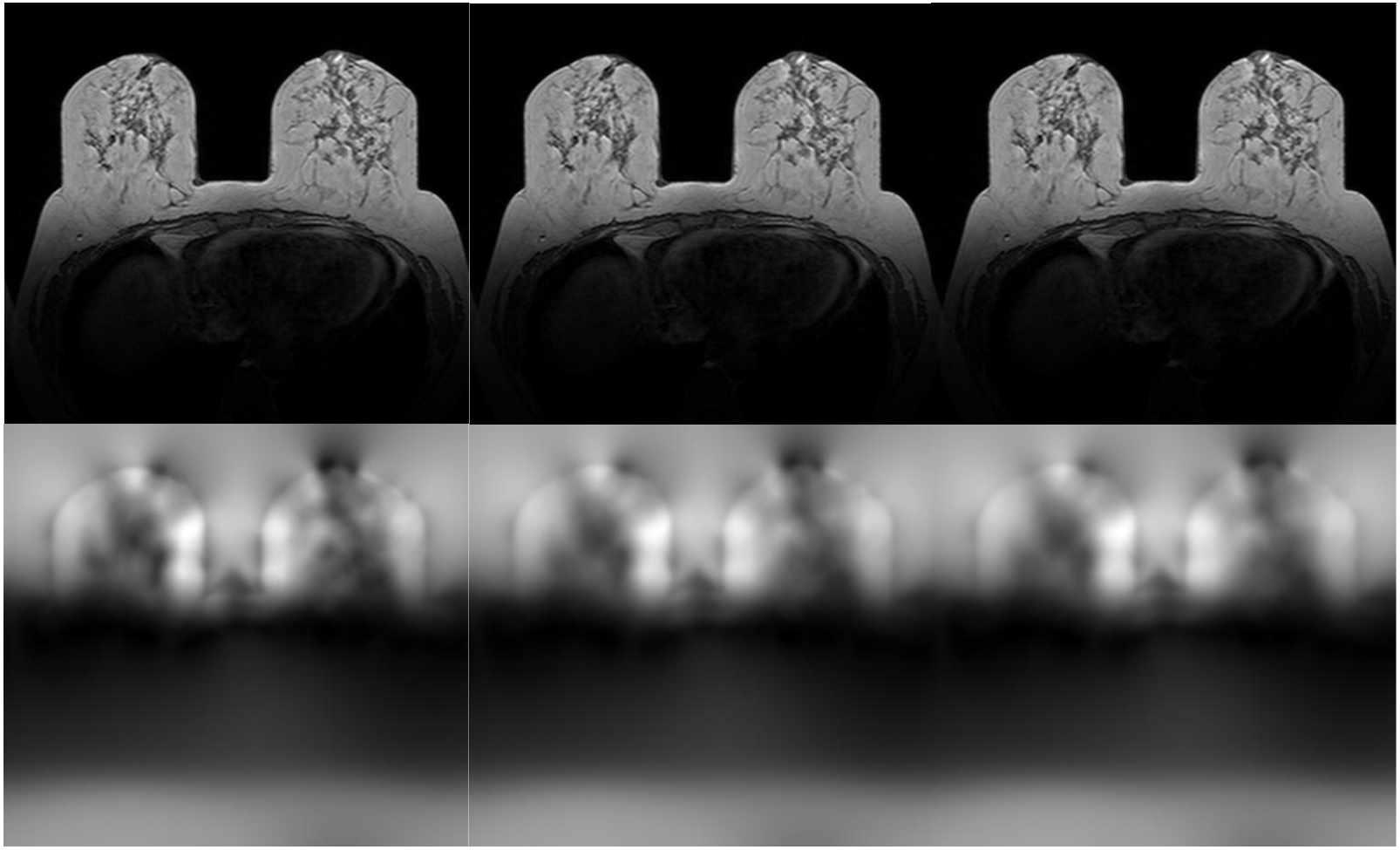

Figure 4.8 Effect of cutoff frequency. On the left column uncorrupted image and bias image is obtained at 0.024, in the middle uncorrupted image and bias field is obtained at optimum cutoff frequency, 0.028; and on the right uncorrupted image and bias image is obtained at 0.032.

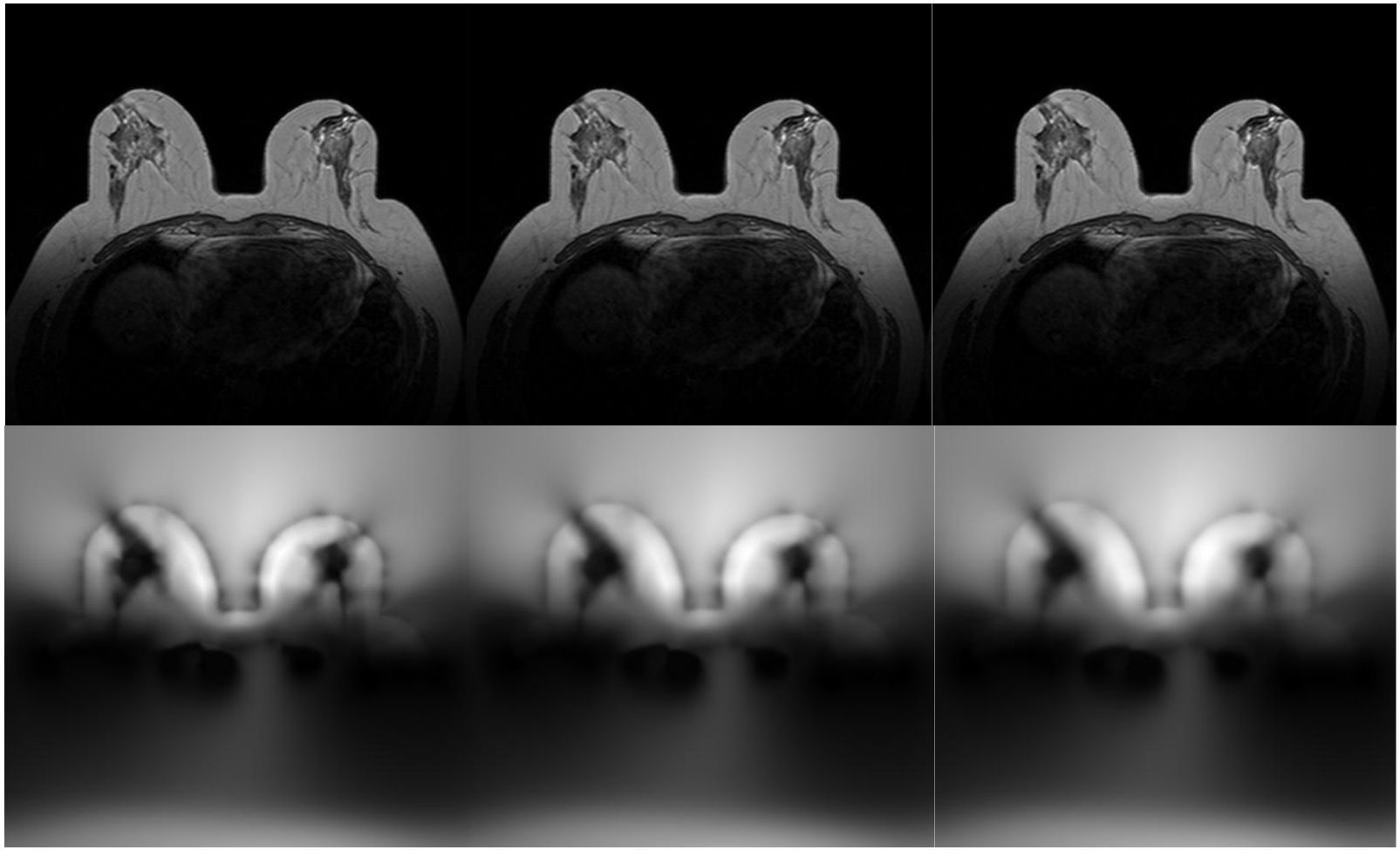

Figure 4.9 On the left column uncorrupted image and the bias field is obtained at 0.016; in the middle uncorrupted image and the bias filed is obtained at the optimum cutoff frequency 0.020; and on the right uncorrupted image and the bias field is obtained at 0.024.

5. DISCUSSIONS AND CONCLUSIONS

5.1 General Discussions

The incidence of breast cancer is slowly increasing worldwide; in developed nations women have a lifetime breast cancer risk of approximately 1 in 12 [1]. The incidence of breast cancer steadily increases with age, starting from 40 years. With the introduction of mammographic breast screening programs, earlier detection combined with improved and adjuvant treatments have resulted in a decline in breast cancer mortality rates.

Conventional methods of detecting, diagnosing, and staging intramammary breast malignancy include the combination of screen-film X-ray mammography, high-resolution breast ultrasonography (US), and clinical breast examination. They account for approximately 85-90% of breast malignancies detected. However conventional methods may fail in cases where there is a palpable lesion without a focal imaging correlate, in interval cancers that are missed or not visible on initial images, in patients presenting with distant or axillary breast cancer metastasis with no breast lesion found on mammograms or sonograms, in cases where chest wall invasion is not detected, in clinical assessment of large tumors that are treated with neoadjuvant chemotherapy, etc. In these situations Magnetic Resonance Mammography (MRM) can be used as an adjuct diagnostic tool due to its high sensitivity. The basis of this high sensitivity is due to the tumor angiogenesis that accompanies a majority of breast cancers, even early ones that accompany secretion of factors such as vascular endothelial growth factor (VEGF), which in turn is strongly correlated with contrast enhancement.

The advantages of MRM over conventional breast imaging for the detection of malignancy include absence of ionizing radiation, richness of imaging planes, capability of imaging the entire breast volume and chest wall, greater than 90% sensitivity to invasive carcinoma, detection of occult, multifocal, or residual malignancy, accurate size estimation for invasive carcinoma, good spatial resolution and ability to image regional lymph nodes. However, the widespread use of MRM for the detection breast malignancy also has some disadvantages; these include high equipment and

examination costs, limited scanner availability, need for the injection of a contrast agent, poor throughput compared with that of US or mammography, long learning curve for interpretation.

In general, MRM is not performed without conventional imaging first. The following are common agreed-upon and useful indications for MRM; detection of occult breast carcinoma in a patient with carcinoma in an axillary lymph node, evaluation of suspected multifocal or bilateral tumor, evaluation of invasive lobular carcinoma (ILC), characterization of an indeterminate lesion after a full assessment with mammography, US, and physical examination, detection of recurrent breast cancer, detection of occult primary breast carcinoma in the presence of metastatic adenocarcinoma of unknown origin and for monitoring of the response to neoadjuvant chemotherapy.

An important problem in MR mammography is “inhomogeneity”. This term is used to describe anatomically irrelevant intensity variations that may show up throughout the MRM image due to a number of factors, including non-uniformity of the B0 static field, non-linearity of the gradient fields, imperfections in the geometry and the physical properties of the RF coil, problems with the coil tuning, focusing problems, intensity variations in the spin echo and gradient echo pulse sequences, eddy currents which are triggered when the field gradients are switching, noise and/or nonlinearity problems in the electronic circuitry, and complex electromagnetic interactions between the imaged object (breast tissue) and improve the resolution of the images for precise diagnosis. A number of methods have been proposed to minimize and correct for these “inhomogeneities” caused by the aforementioned factors within the acquired MR images. However, most of these techniques require either user interaction and/or prior tissue information and have been specifically developed for brain MR images. The authors have not been able to find a correction scheme developed especially for breast MR images.

5.2 Conclusions

Correction of “inhomogeneity” in MRM is very important for improving resolution of the images and thus improving discrimination between benign and

malignant lesions and for refining treatment strategy. In this thesis we present a novel technique for minimizing these spurious inhomogeneities; to achieve this, we first apply a tissue mask to eliminate filter artifacts, and then apply low-pass filtering to assess the "inhomogeneity". We then obtain a "corrected" image by subtracting this estimated inhomogeneity from of the acquired image.

A frequency range is defined and a number of bias fields and restored images are estimated for each image. Entropy minimization is used to define an optimum cutoff frequency for the low-pass filter. This results in a fast, user independent, nonparametric algorithm. The method is demonstrated on various breast images from different patients. A performance evaluation method is also defined for quantitative measurement.

Despite the optimization procedure that is required, the method proposed in this thesis work is promising, since it is non-parametric, and not model-based. Furthermore, it does not require user control. A main problem of the inhomogeneity correction methods that have been reported in the literature is that, they need tissue parameters or a tissue model for bias field estimation. These techniques are suitable for brain MR images, which can be modeled, and have distinct intensity value classes corresponding to say the gray matter or the white matter areas. Unfortunately, this is not possible for the breast. Therefore, performance of these methods on breast MR images is not properly evaluated, and requires further research.

5.3 Suggestions for Furtherwork

MR images are usually corrupted by smoothly varying bias field that affects the performance of the image analysis, segmentation and registration systems and may lead to misdiagnosis. Sources of the bias field may be the inhomogeneity of the static magnetic field, inhomogeneity of the secondary magnetic field and nonuniformity of the receiver coil. Calibration of the system generally does not result in removal of this bias field, hence post-processing techniques, in general, are required to minimize its effects.

It is difficult, in general, to fit MR mammogram images into a single model like the brain MR images since tissue properties vary from patient-to-patient and thus it is not possible immediately to identify the distinct tissue regions (such as white matter or

gray matter). Therefore in the present thesis work we propose a method based on modified homomorphic filtering that does not require any model or prior knowledge of distinct tissue classes [21]. Since this method requires user control to define the cutoff frequency, an optimization is performed based on Mangin's entropy minimization technique [19]. A cost function, $J(f_c)$ that depends on the corrected image's entropy, smoothness of the bias field and the square of the difference of the mean of the original and the corrected images. The minimum of the cost function gives the optimum cutoff frequency of the filter.

The results of this work indicate that, for the given image set, the proposed method properly minimizes cost function, $J(f_c)$ and estimates an optimum cutoff frequency for most images, independent from the tissue properties. In fact tissue properties have no effect on the minimization.

For the estimated cutoff frequencies the bias field is minimized properly. The inner structures are preserved in the uncorrupted images. Fatty and the fibrous tissues become more discriminable when the fibrous tissue exhibits netty structure. Also the chest wall and the breast tissues close to it and the body become more visible. This will results lead better screening and hence better diagnosis.

In addition to these, since intensity variations decrease, it may result in a better performance of the segmentation and registration algorithms, which is the main objective of correction methods.

One of the main problems of the proposed method is estimating an optimum cutoff frequency when there is no minimum value of $J(f_c)$. Our results indicate that when the slope of the $J(f_c)$ decreases and it tends to have relatively flat regions, the cutoff frequencies at these regions are also the optimum. Since we only look for a minima of the functions, other search method that can also find these relatively flat regions may increase the performance of the method.

As Guillemaud et al. [15] showed tissue masking prevents edge artifacts between breast and background. However when the fibrous tissue spreads and exhibit netty

structure, artifacts occur in and around the fibrous tissue undesirably. In our method grey-level histogram thresholding is used to obtain the tissue mask. This method estimates an optimum threshold value between the two peak values of the histogram. Since the objective of tissue masking is to define edges properly, and preventing edge artifacts, more sophisticated methods should be used to define not only breast – background borders, but also the borders of different tissue types (such as fat – fibrous tissue). Another issue is that, grey-level histogram thresholding method fails to estimate the breast region properly, when the intensity value is relatively low. Hence the use of a better tissue mask should covering the breast region more accurately, may result in a better estimation of the bias field, consequently better correction results.

In the present work and also in the literature, in general, the effect of the noise is neglected, since the S/N ratio is quite good. However, this noise may be effective on the estimation of the bias field and on the performance of thresholding. As a result the effect of the noise should be investigated. Prefiltering of the noise before processing may also increase the performance.

APPENDIX A

Figure A.1 belongs to a patient with malignant findings (Patient 7, Slice 6). As shown in this figure, the image contains almost no fibrous tissue. The figure on the left is the original mammogram and that in the right is the corrected mammogram. It can be seen the as the effect of the bias field is removed, the chest wall and the inner body structures become visible.

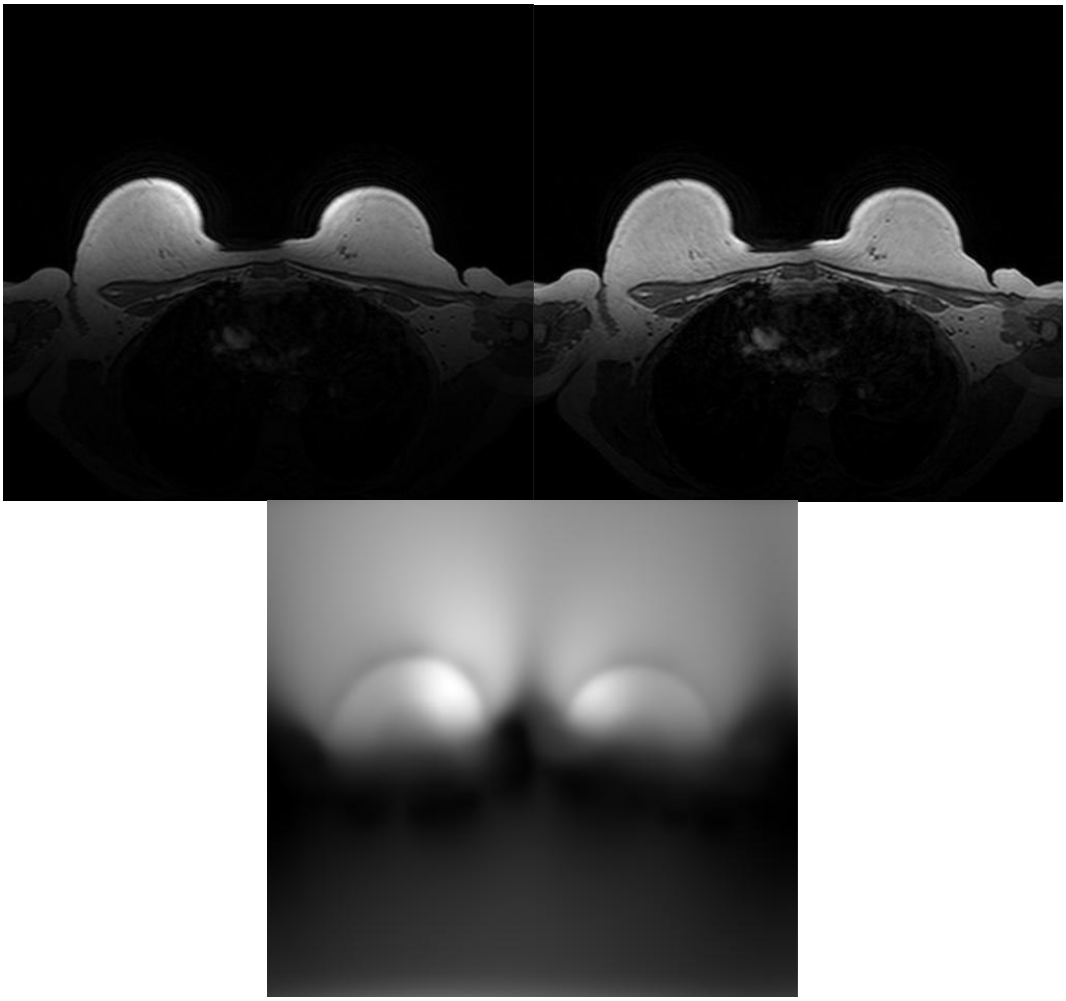

Figure A.1 Estimated cutoff = 0.040, average information loss, E = 0.0021

Figure A.2 belongs to another patient with malignant findings (Patient 4, Slice 38) and with almost no fibrous tissue. Again, the figure on the left is the original mammogram and that in the right is the corrected mammogram. It is seen the as the effect of the bias field is removed, the chest wall and the inner body structures become visible.

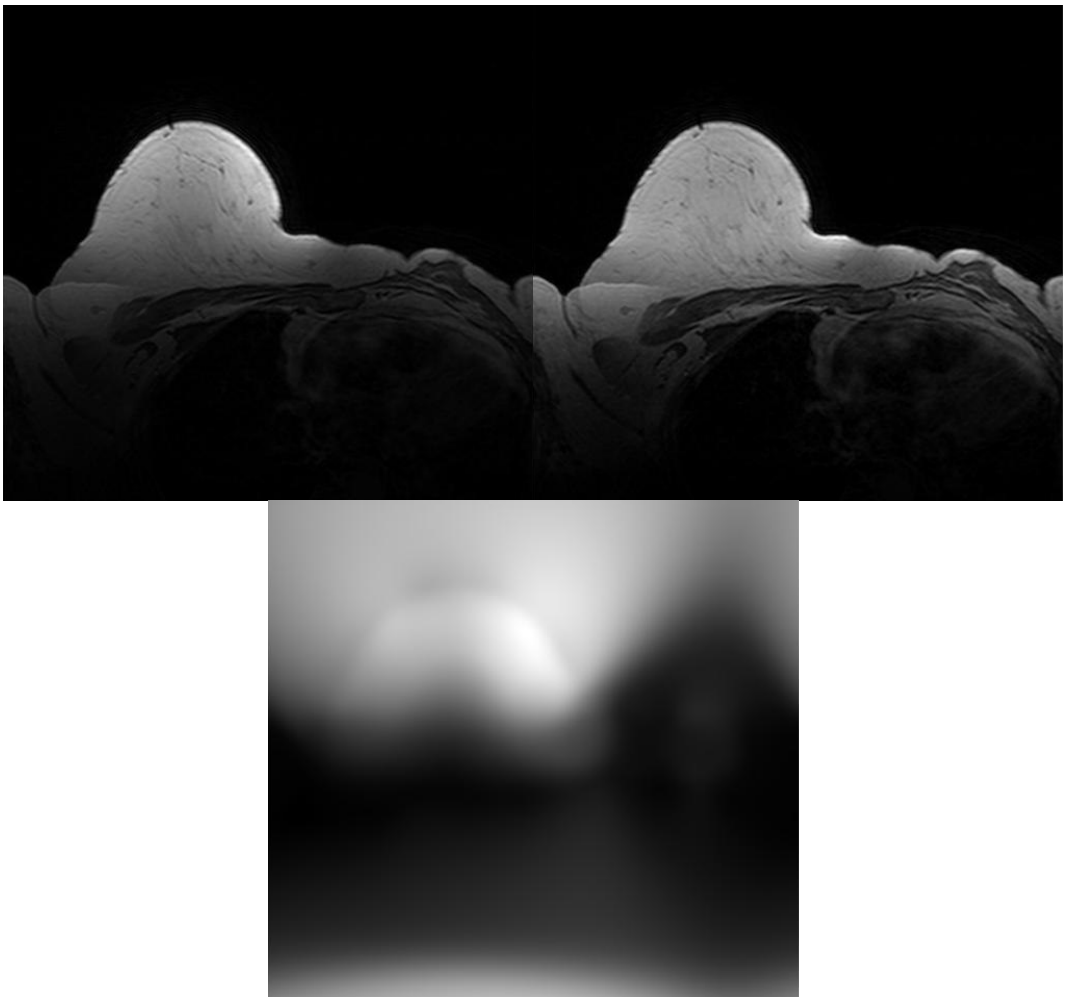

Figure A.2 Estimated cutoff = 0.062, average information loss, E = 0.0032

Figure A3 belongs to patient with malignant findings, and with both fatty and fibrous tissue (Patient 9, Slice 12). The figure on the left is the original mammogram and that in the right is the corrected mammogram. It is seen as the effect of the bias field is removed, the chest wall and the inner body structures become visible.

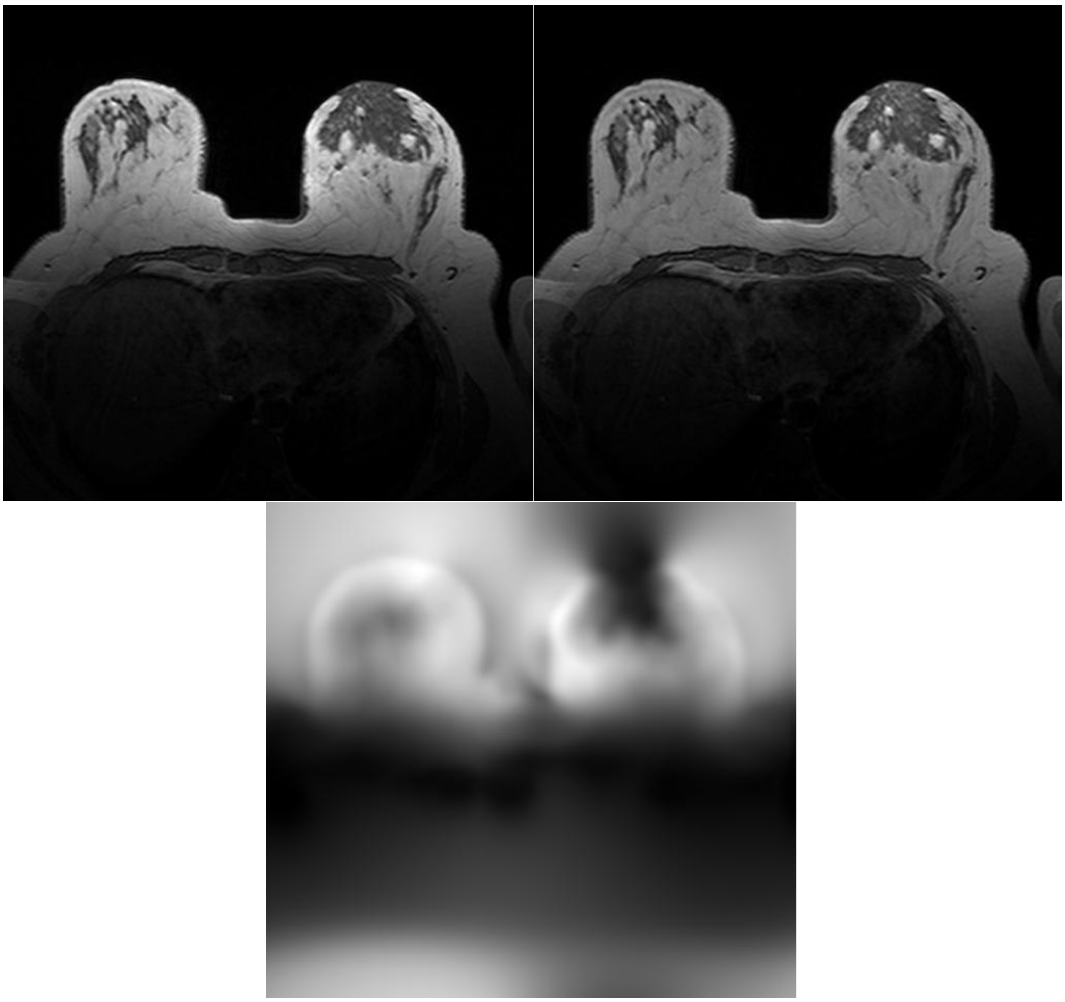

Figure A.3 Estimated cutoff = 0.042, average information loss, E = 0.0036

Figure A.4 belongs to Patient 9 (Slice 22). In the uncorrupted image fibrous tissue and fatty tissue become discriminable, and the chest wall and other structures become visible. When the bias field is removed properly, the inhomogeneity corrected image has almost no edge artifacts around fibrous tissue.

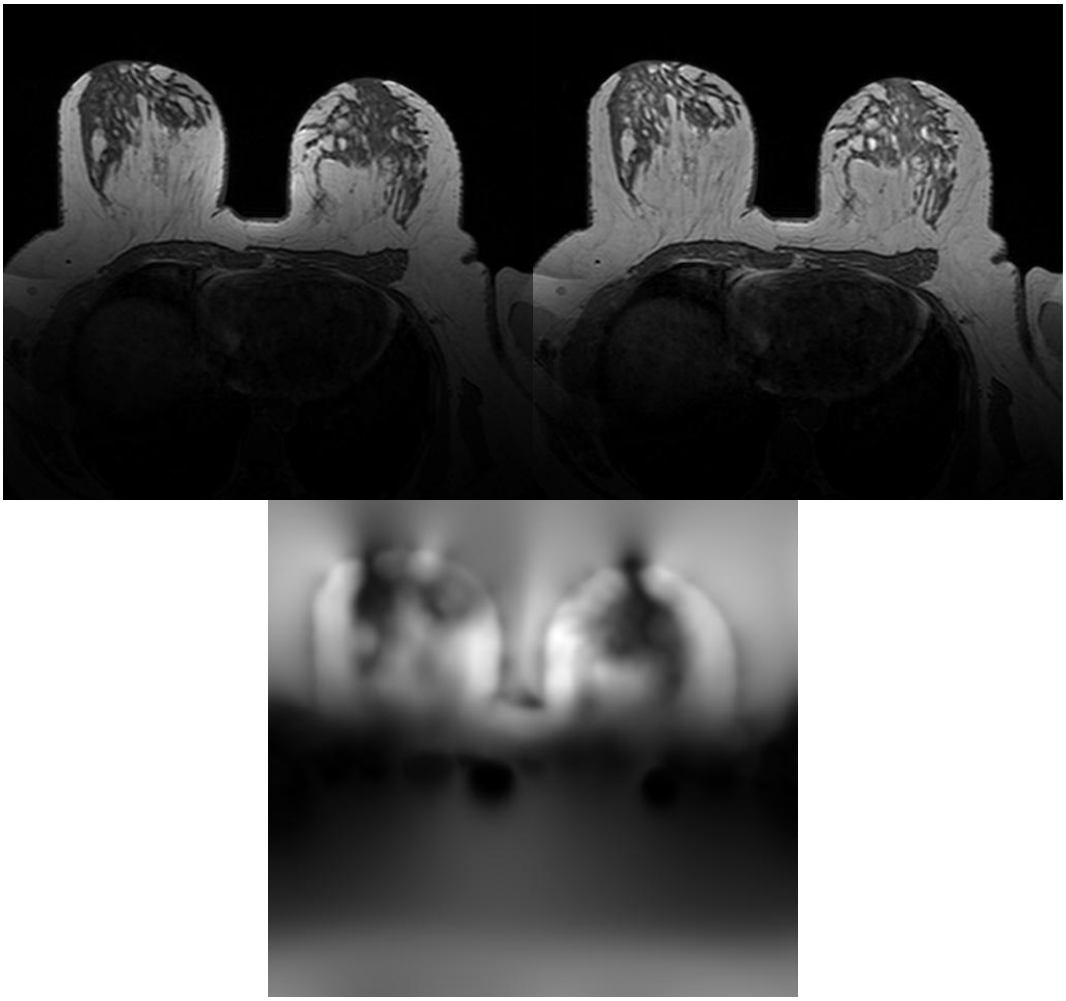

Figure A.4 Estimated cutoff = 0.026, average information loss, E = 0.0048

Figure A.5 belongs to a healthy individual having no fibrous tissue in the mammogram (Patient 10, Slice 38). When the bias field inhomogeneity is corrected (figure on the right), the breast contour and the chest wall becomes more visible.

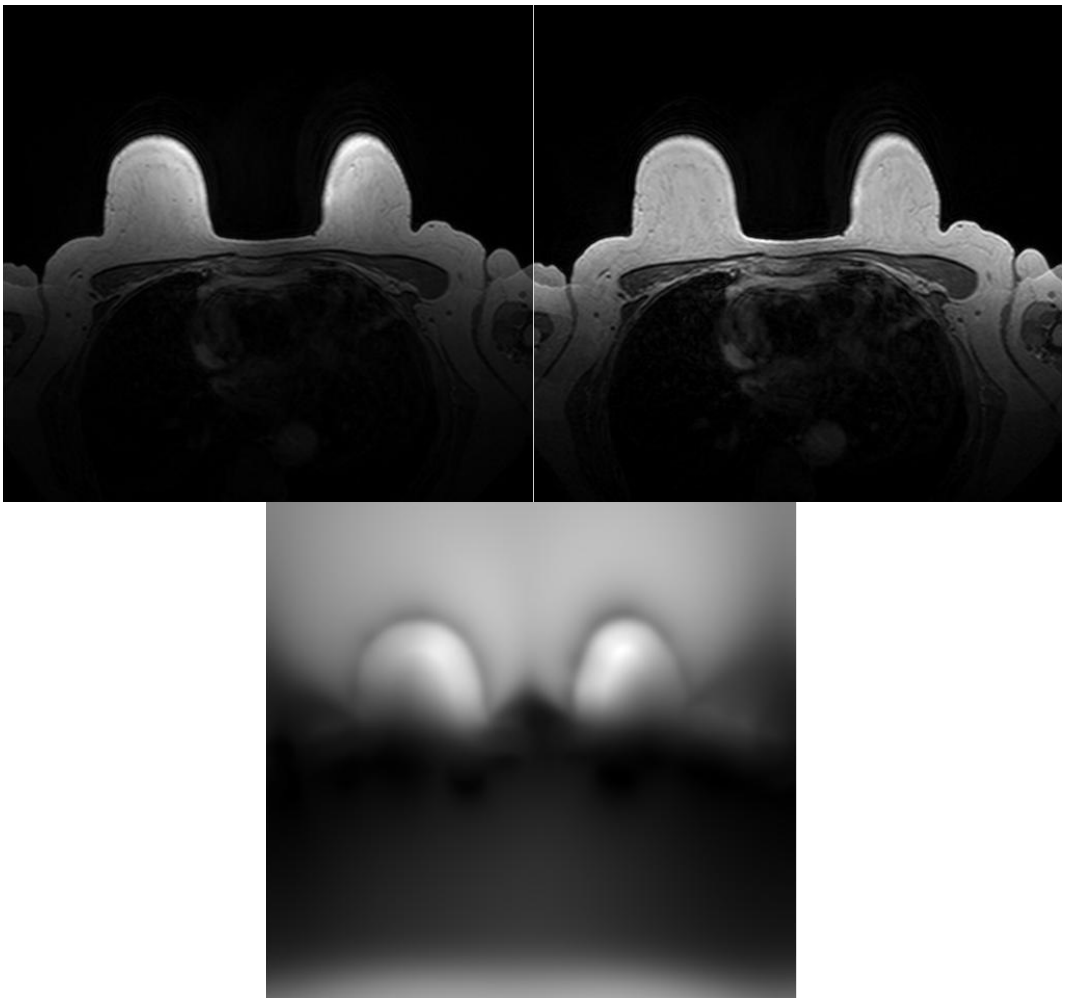

Figure A.5 Estimated cutoff = 0.030, average information loss, E = 0.0055

Figure A.6 shows the MR mammogram of Patient 1, Slice 32. Figure on the right shows the field inhomogeneity corrected mammogram. Note that "bright" spots are reduced.

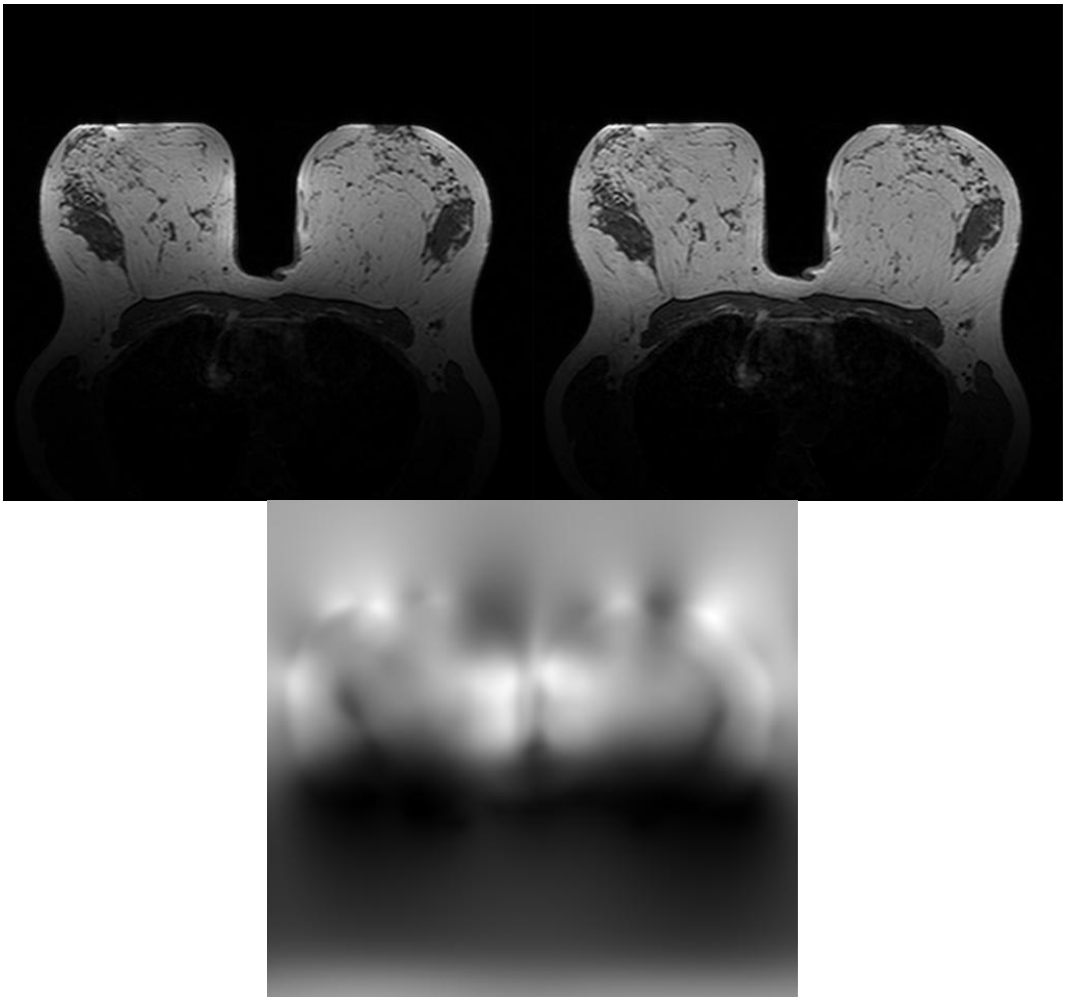

Figure A.6 Estimated cutoff = 0.040, average information loss, E = 0.0028

Figure A.7 belongs to a patient with benign findings (Patient 1, Slice 12). Figure on the right is the bias field inhomogeneity corrected image. Bright spots on the breast contours are reduced. The corrected image has more detailed view of the chest wall and the body.

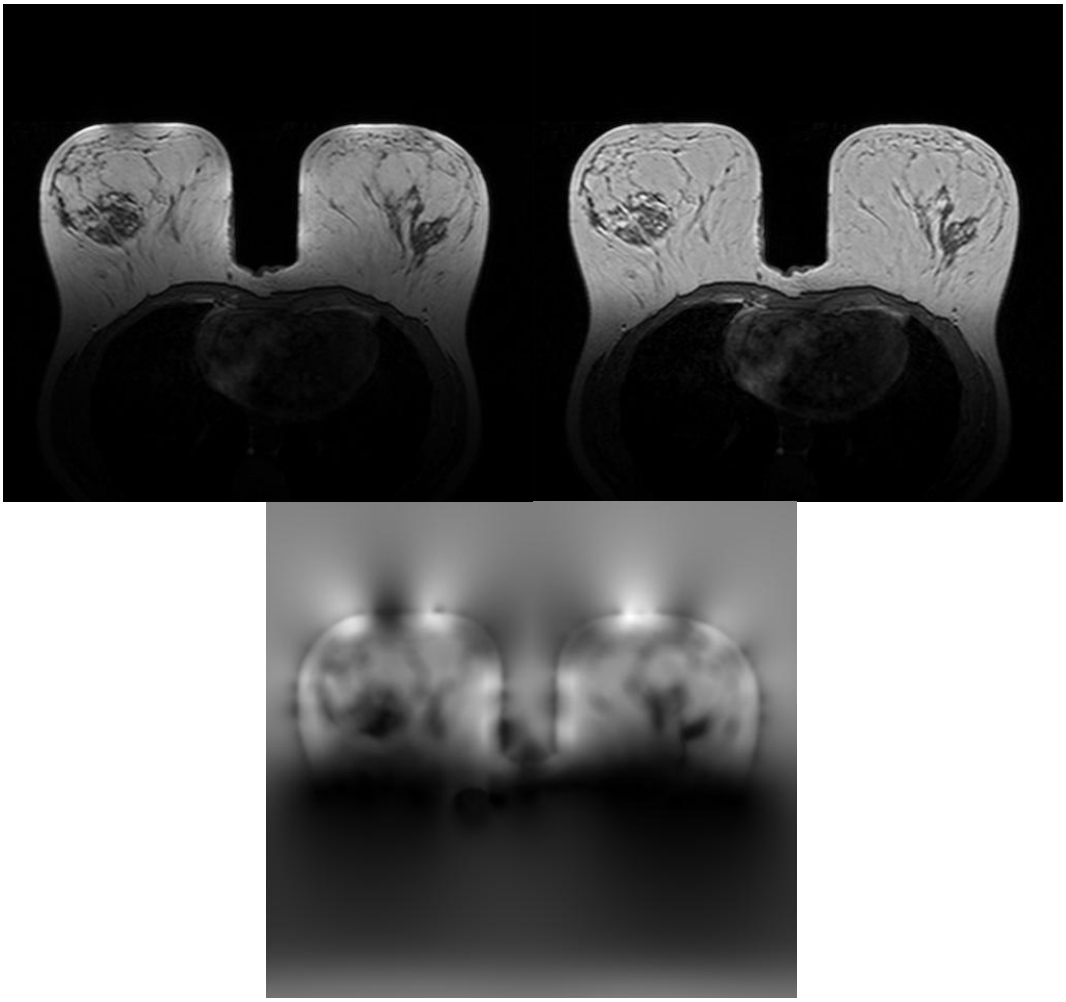

Figure A.7 Estimated cutoff = 0.016, average information loss, E = 0.0048

Figure A.8 belongs to a healthy individual (Patient 2, Slice12). The figure on the right is the bias field inhomogeneity corrected image. The inner structures and the chest wall become visible. However edge artifacts occur on the tissue boundaries, since the tissue mask cannot properly obtained.

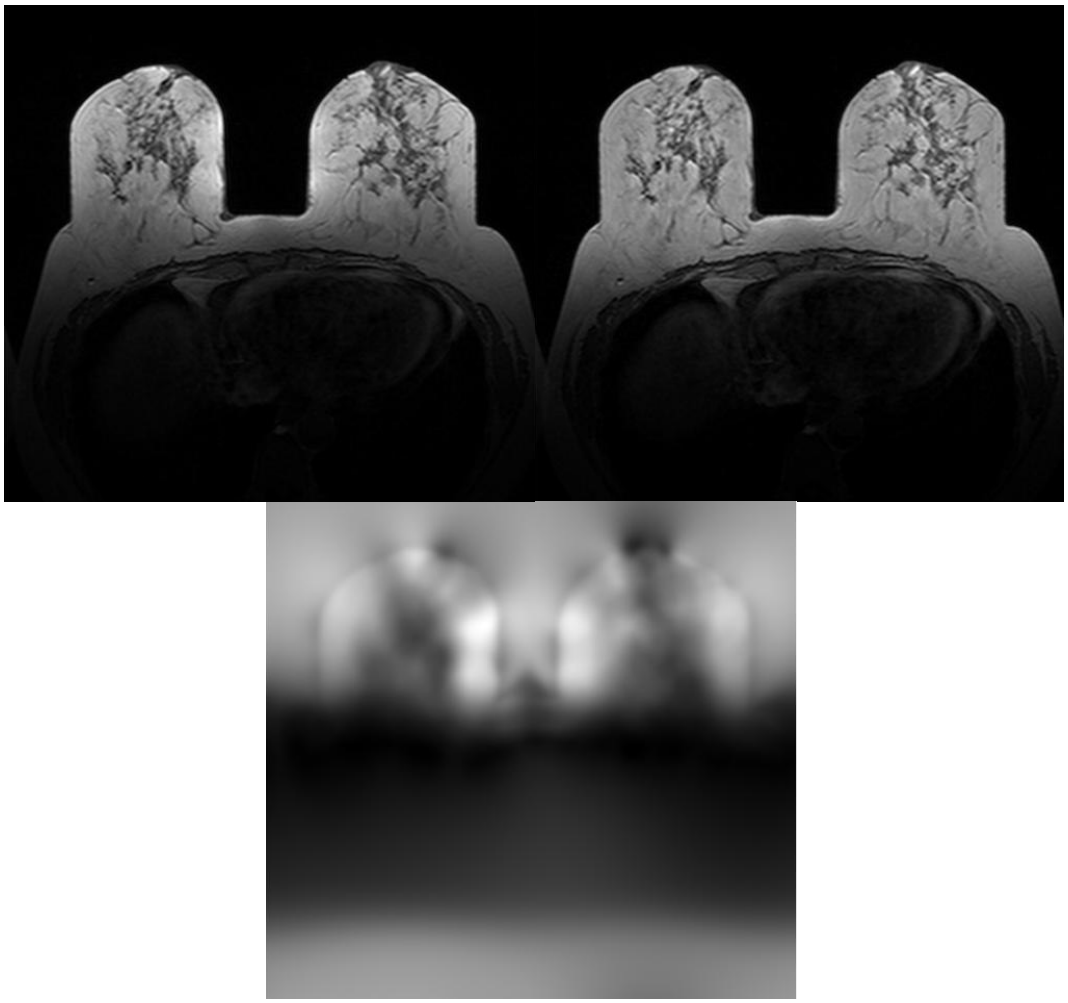

Figure A.8 Estimated cutoff = 0.030, average information loss, E = 0.0039

Figure A.9 belongs to a healthy individual (Patient 2, Slice 32). Figure on the right is the bias field inhomogeneity corrected image and has a detailed view of the chest wall and the body. Since tissue mask is obtained properly, there is no edge artifact on the tissue boundaries. Furthermore, bias field inhomogeneity on the breast contour is minimized.

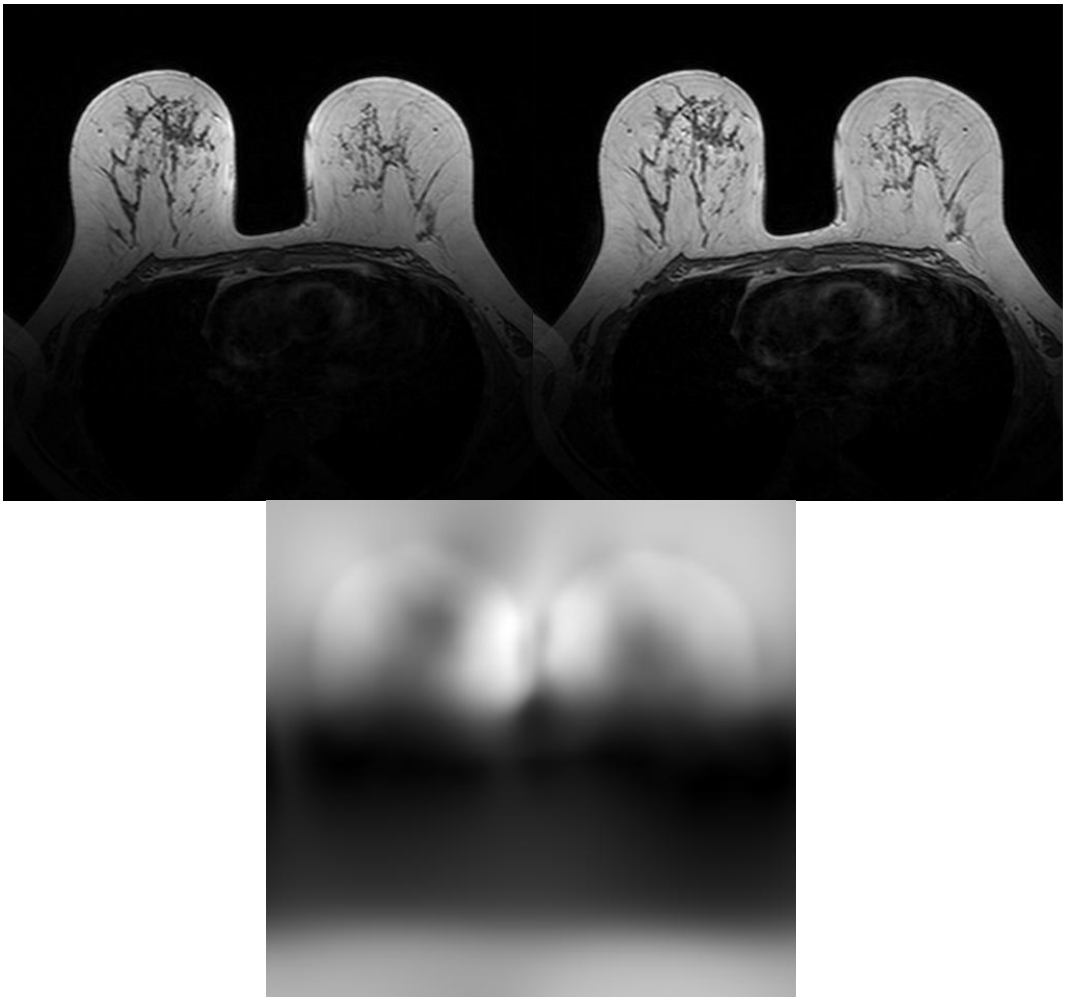

Figure A.9 Estimated cutoff = 0.048, average information loss, E = 0.0023

Figure A.10 belongs to a patient with malignant findings (Patient 3, Slice 12). The bias field inhomogeneity corrected image (figure on the right) has more details of the inner structures and the tissues are more discriminable. Furthermore, the bias field inhomogeneity (bright spots on the breast contour) is minimized. However edge artifacts occur between different tissue types.

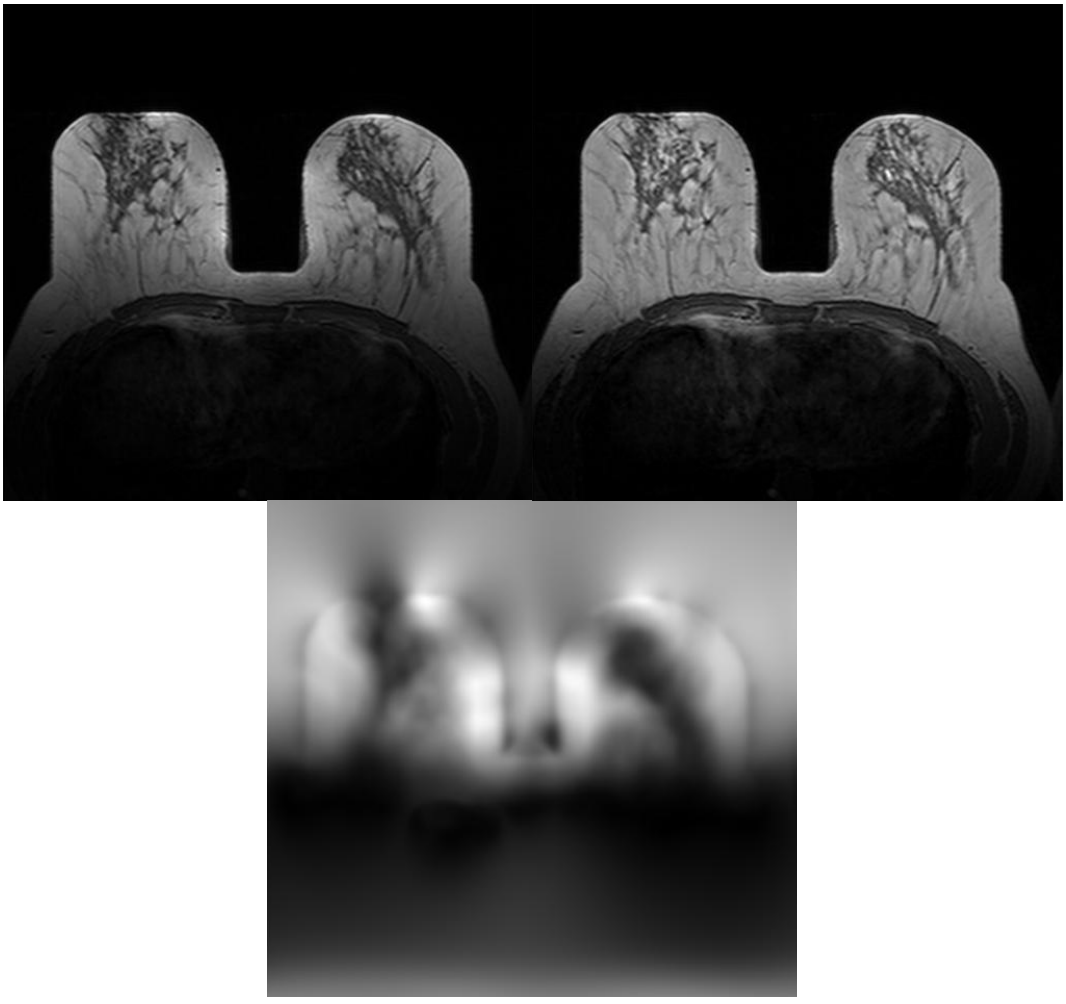

Figure A.10 Estimated cutoff = 0.028, average information loss, E = 0.0051

Figure A.11 belongs to Patient 3 again (Slice 38). Unlike Figure A.10, the bias field inhomogeneity corrected image (figure on the right) has no visible edge artifacts between different tissue types. When the bias field inhomogeneity is corrected, the chest wall and the body become more visible.

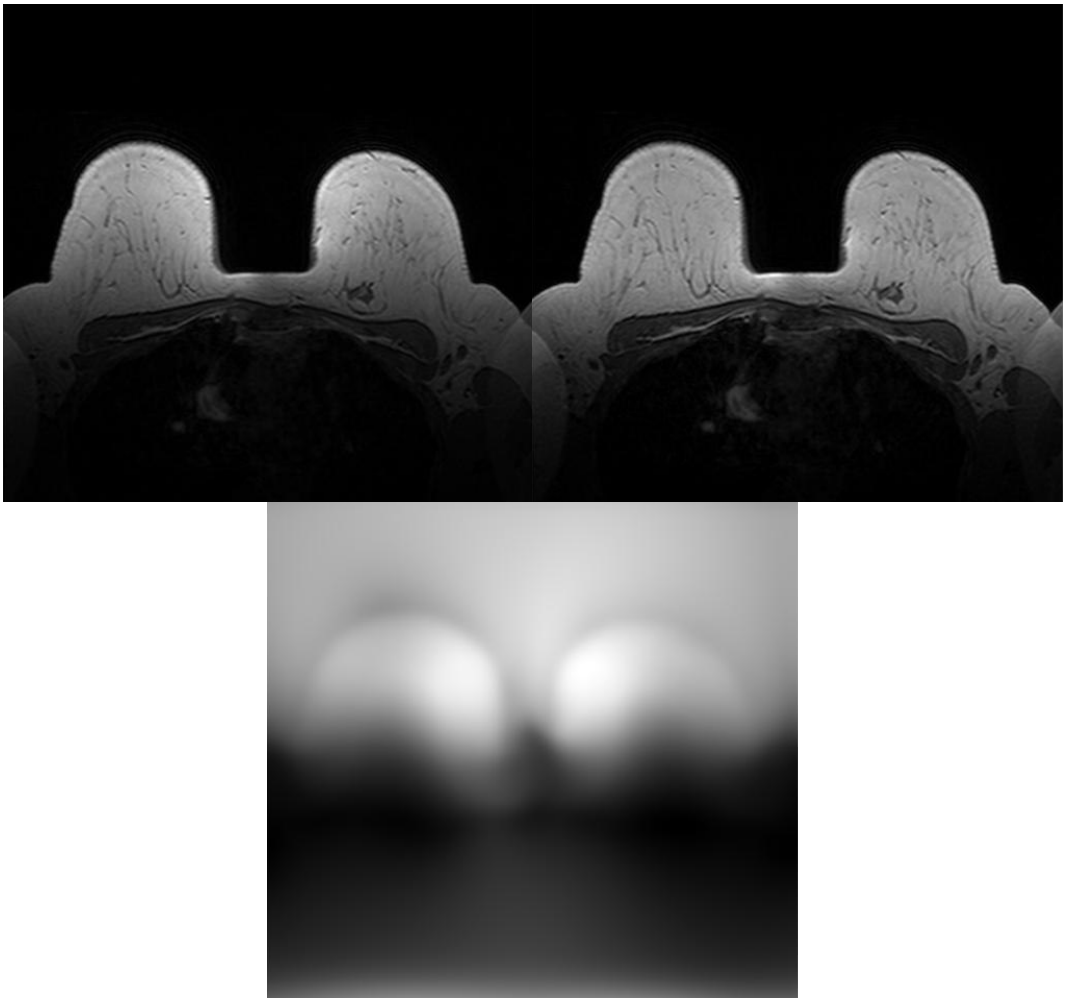

Figure A.11 Estimated cutoff = 0.060, average information loss, E = 0.0034

Figure A.12 belongs to a patient with malignant findings (Patient 4, Slice 12). The streak bias field inhomogeneity that affects the most part of the breast is minimized. Furthermore, corrected image has more discriminable view of the inner structures and the chest wall becomes more visible.

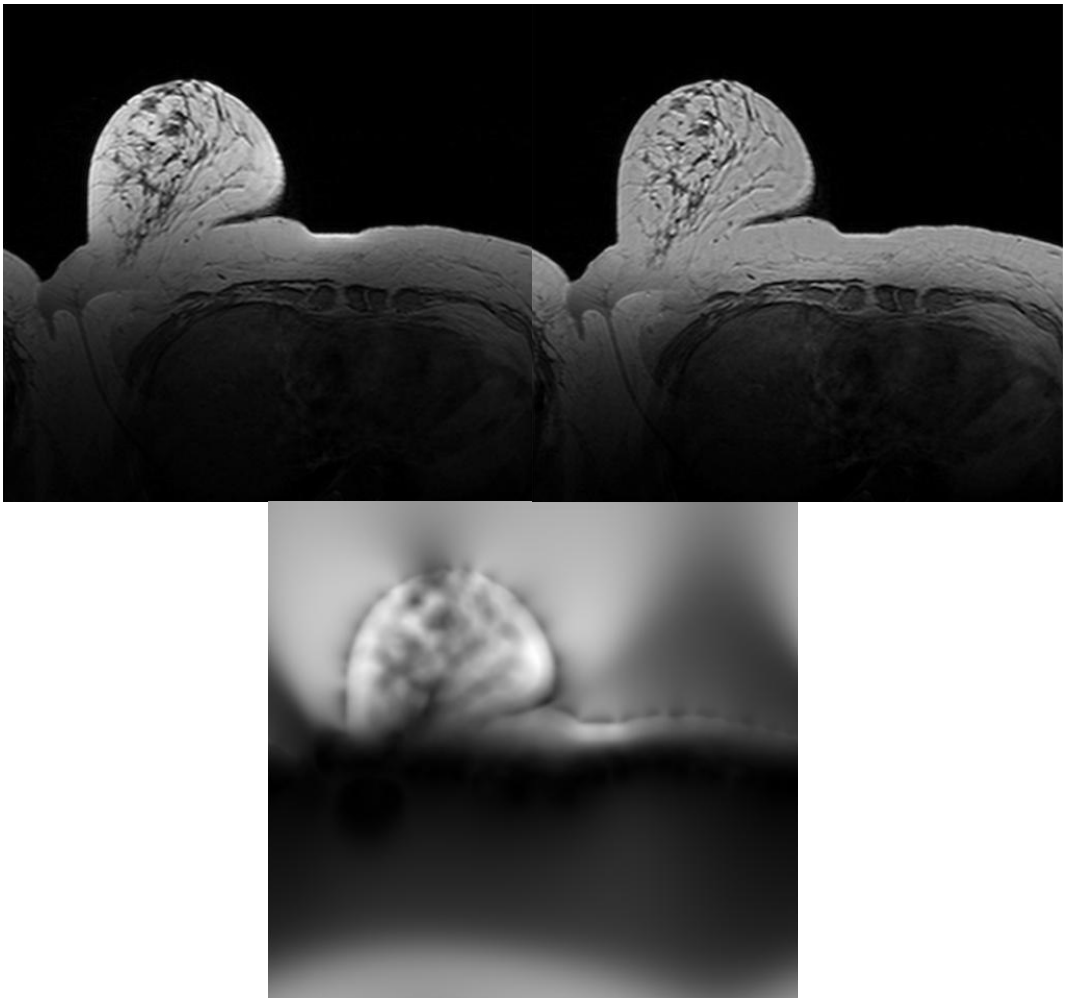

Figure A.12 Estimated cutoff = 0.016, average information loss, E = 0.0065

Figure A.13 belongs to Patient 4 again (Slice 22). Figure on the right is the bias field inhomogeneity corrected image and that on the left is the original image. As it is seen on the corrected image, the inner structures lost details. However the bias field inhomogeneity is minimized.

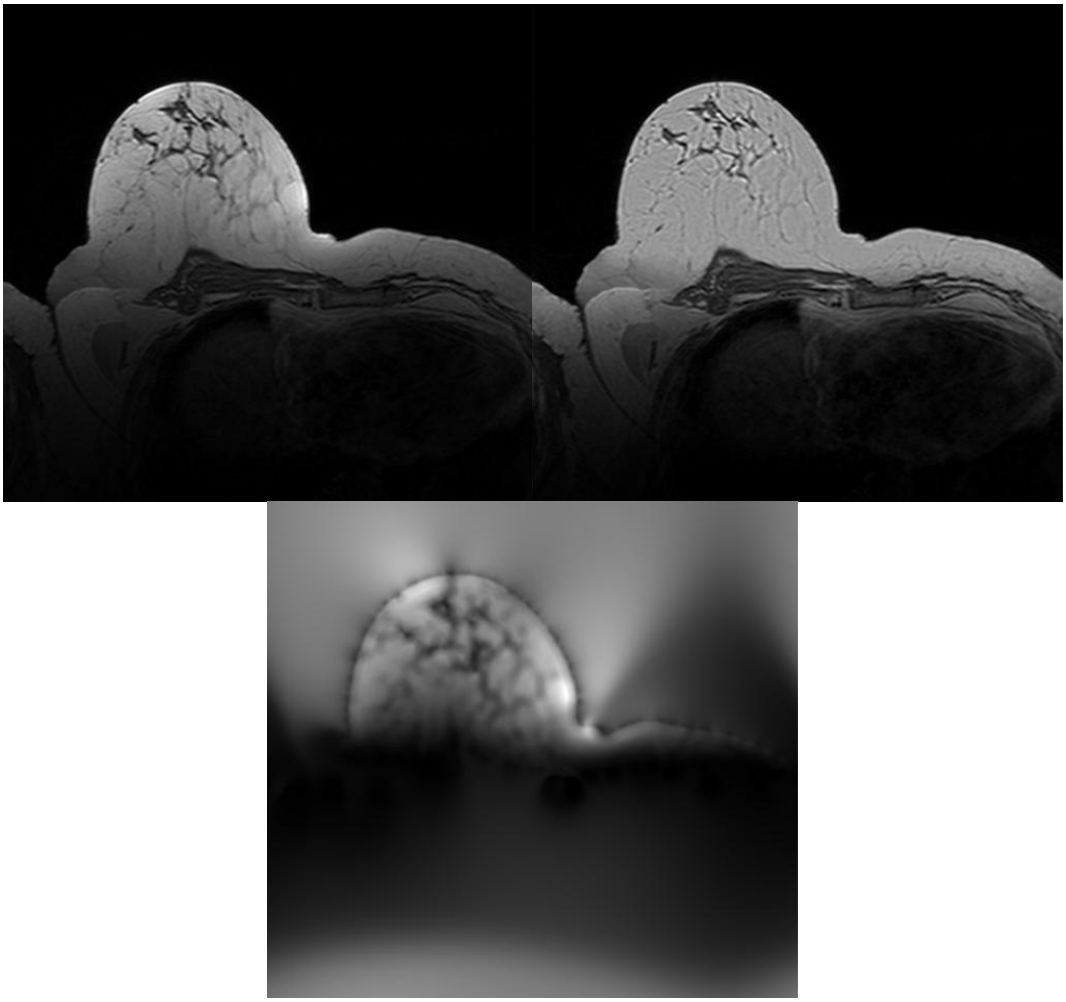

Figure A.13 Estimated cutoff = 0.010, average information loss, E = 0.0071

Figure A.14 belongs to a patient with benign findings (Patient 5, Slice 6). The bias field inhomogeneity corrected image is on the right and that on the left is the original image. The chest wall and the body become more visible in the corrected image.

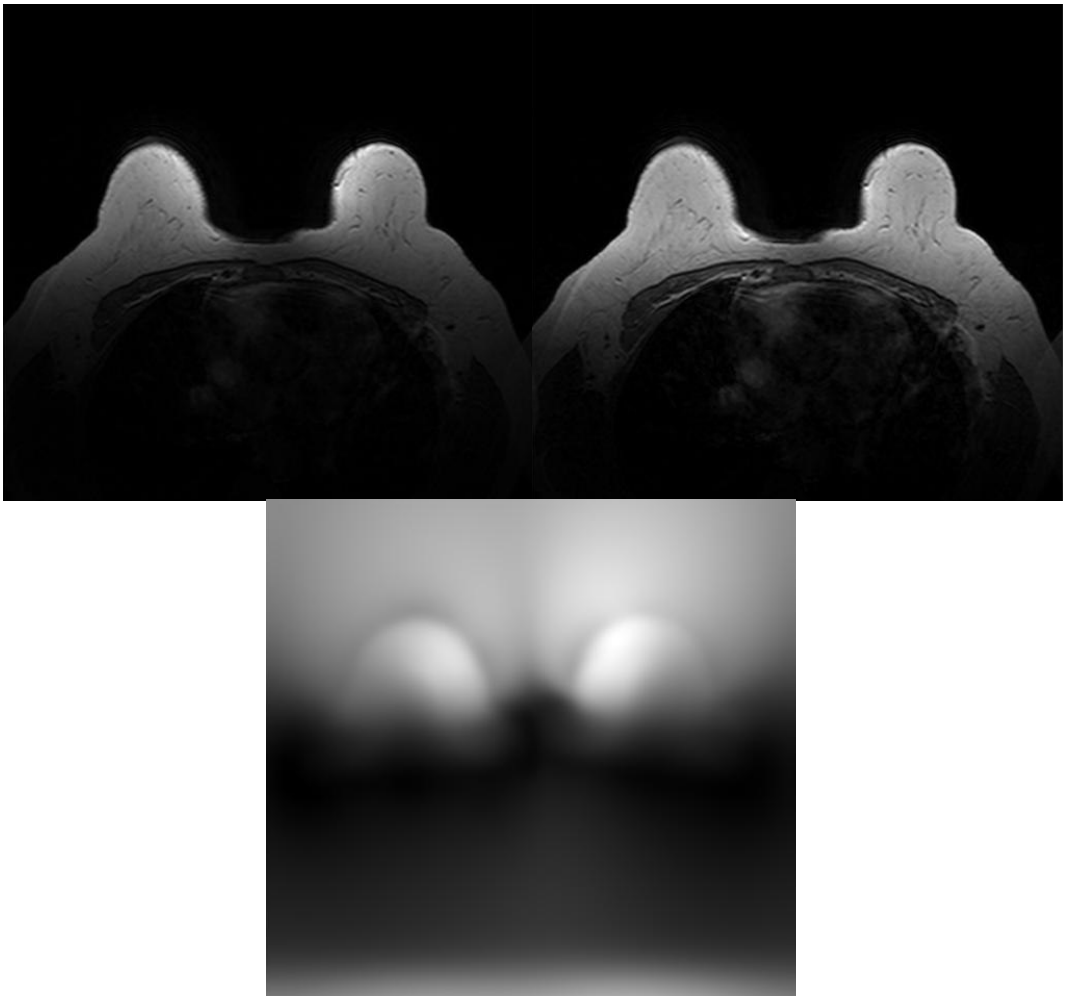

Figure A.14 Estimated cutoff = 0.050, average information loss, E = 0.0044

Figure A.15 belongs to a patient with malignant findings (Patient 7, Slice 12). Figure on the right is the bias field inhomogeneity corrected image. When the bias field is corrected, the chest wall and the body become more visible. Since the tissue mask is obtained properly there is no edge artifact on the tissue boundaries.

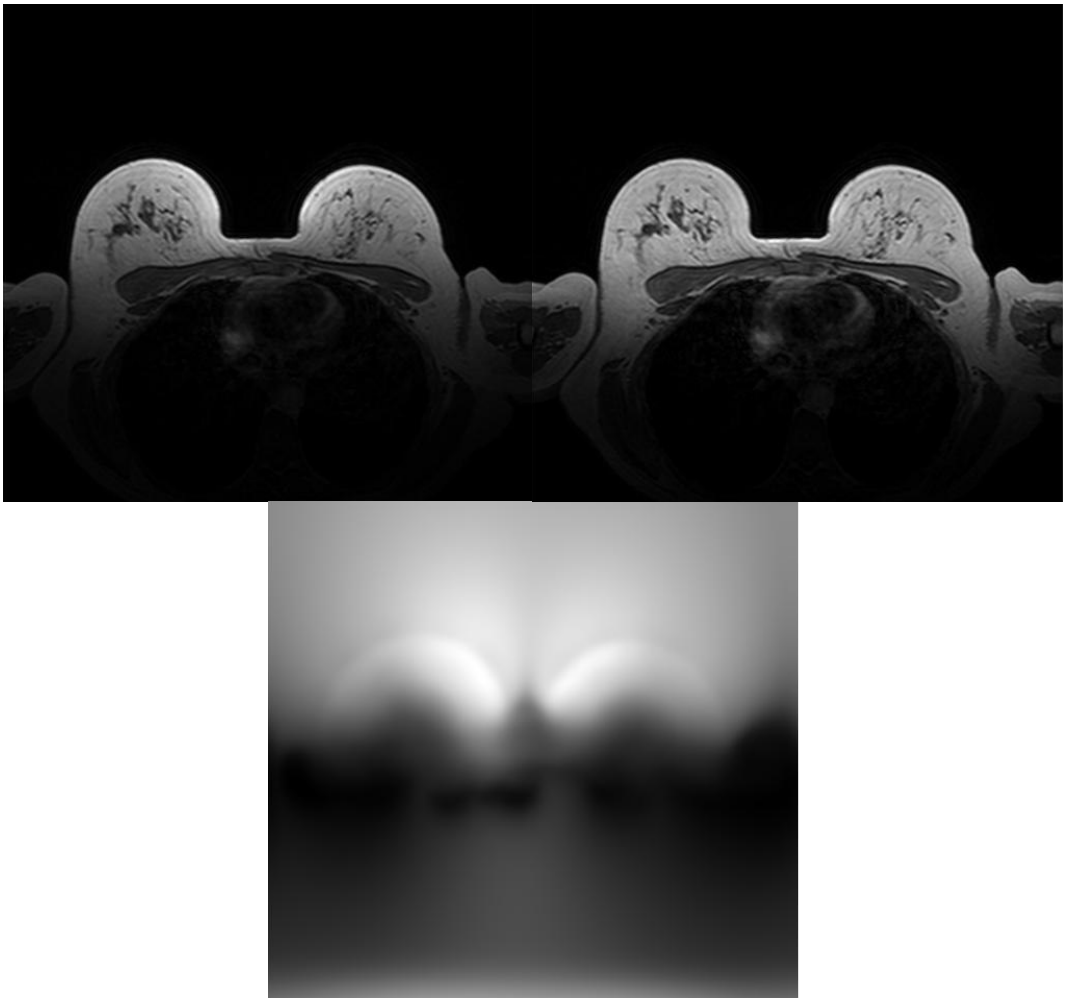

Figure A.15 Estimated cutoff = 0.046, average information loss, E = 0.0020

Figure A.16 belongs to a healthy individual (Patient 8, Slice 6). Since the chest wall and the body become more visible in the bias field corrected image (figure on the right), fibrous tissue around the chest wall and the body also become more visible. Furthermore, corrected image has no edge artifacts between different tissue types.

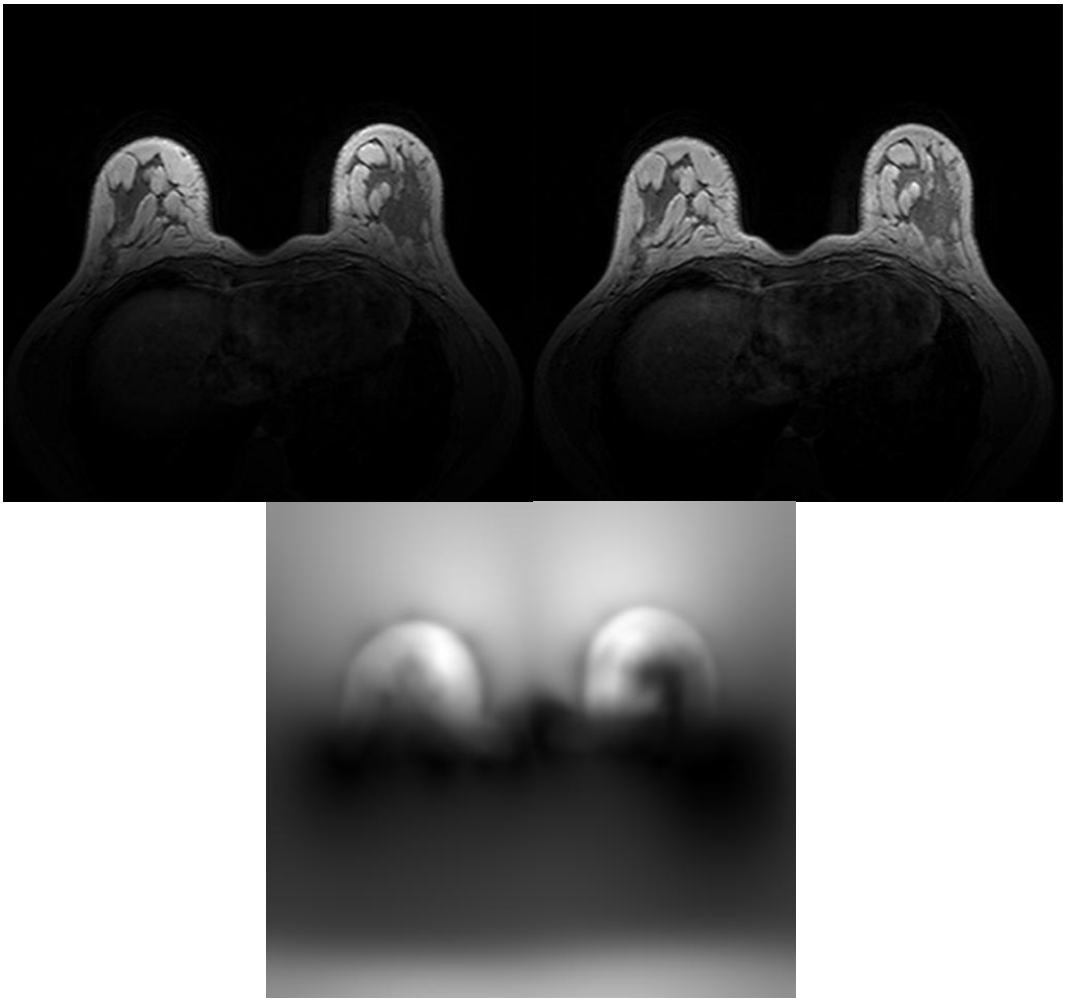

Figure A.16 Estimated cutoff = 0.030, average information loss, E = 0.0024

Figure A.17 belongs to Patient 8 again (Slice 23). As figure A.16 the fibrous tissue around the chest wall and the body become more visible. However the corrected image (figure on the right) has edge artifacts on the tissue boundaries.

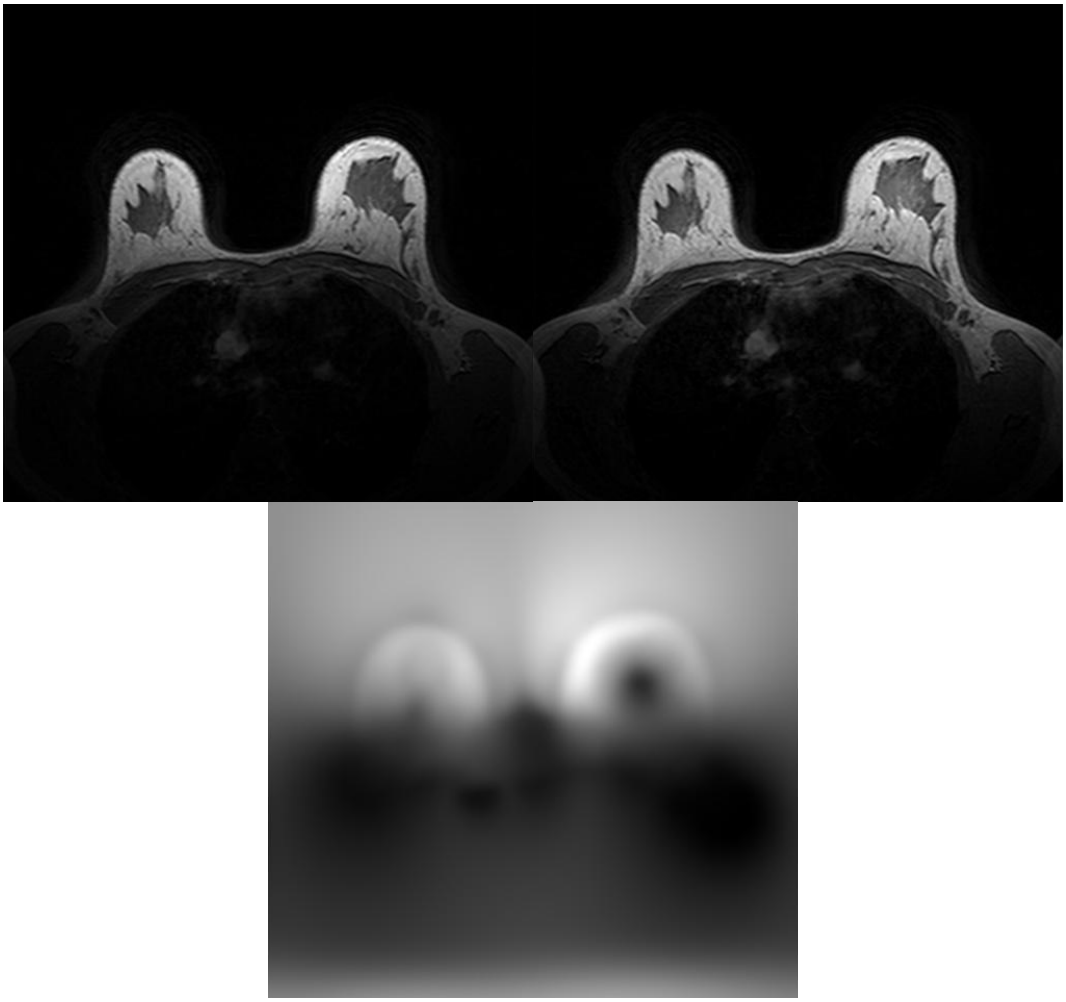

Figure A.17 Estimated cutoff = 0.050, average information loss, E = 0.0014

REFERENCES

1. Dilulio, R., "Step by step – The highs and lows of breast MR", *Medical Imaging,* 2005. Available: http://www.medicalimagingmag.com.
2. Wang, S.-C. and R. L. Birdwell "Magnetic resonance mammography" *eMedicine*, August 2004, Available: http://www.emedicine.com/radio/topic792.htm
3. Shah, S. K., Shah, S. K., Greatrex, K. V., "Current role of magnetic resonance imaging in breast imaging: A primer for the primary care physician", 2005. Available: http://www.medscape.com.
4. Reinikainen, H., "Complementary imaging of solid breast lesions", 2003. Available: http://herkules.oulu.fi.
5. Lewis, E. B., Fox, N. C., "Correction of differential intensity inhomogeneity in longitudinal MR images," *NeuroImage*, 23, pp. 75-83, 2004.
6. Vlaardingerbroek, M. T., den Boer, J. A., *Magnetic Resonance Imaging: Theory and Practice*, Springer, 2003.
7. Chen, W., Giger, M. L., "A fuzzy c-means (FCM) based algorithm for intensity inhomogeneity correction and segmentation of MR images," *IEEE International Symposium on Biomedical Imaging, ,*2004.
8. Vovk, U., Pernuš, F., Likar, B., "MRI intensity inhomogeneity correction by combining intensity and spatial information," *Physics in Medicine and Biology*, 49, pp. 4119-4133, 2004.
9. Vokurka, E. A., Thacker, N. A., Jackson, A., "A fast model independent method for automatic correction of intensity nonuniformity in MRI data," *Magnetic Resonance Imaging,* vol. 10, pp. 550-562, 1999.
10. Sled, J. G., Zijdenbos, A.P., Evans, A. C., "A nonparametric method for automatic correction of intensity nonuniformity in MRI data," *IEEE Transactions on Medical Imaging*, vol. 17, no. 1, pp. 87-97, February 1998.
11. Leemput, K. V., Faes, M., Vandermeulen, D., Suetens, P., "Automated model-Based bias field correction of MR images of the brain," *IEEE Transactions on Medical Imaging*, vol. 18, no. 10, pp. 885-896, October 1999.
12. Gerig, G., Styner, M., Brechbühler, C., Székely, G., "Parametric estimate of intensity inhomogeneities applied to MRI," *IEEE Transactions on Medical Imaging*, vol. 19, no. 3, pp. 153-165, March 2000.
13. Tincher, M., Meyer, C. R., Gupta, R., Williams, D. M., "Polynomial modeling and reduction of rf body coil spatial inhomogeneity in MRI," *IEEE Transactions on Medical Imaging*, vol. 12, no. 2, pp. 361-365, June 1993.
14. Fan, A. C., *A Variational Approach to MR Bias Correction*. PhD Thesis, University of Minnesota, 2003.
15. Guillemaud, R., Brady, M., "Estimating the Bias Field of MR Images," IEEE Transactions on Medical Imaging, vol. 16, no. 3, pp. 238-251, June 1997.

16. Brinkmann, B. H., Manduca, A., Robb, R. A., "Optimized homomorphic unsharp masking for mr grayscale inhomogeneity correction," *IEEE Transactions on Medical Imaging*, vol. 17, no. 2, pp. 161-171, April 1998.

17. Viola, P., *Alignment by Maximization of Mutual Information*. PhD Thesis, MIT, 1995.

18. Likar, B., Maintz, J. B. A., Viergever, M. A., Pernus, F., "Retrospective shading correction based on entropy minimization," *Journal of Microscopy*, vol. 197, pt. 3, pp. 285-295, March 2000.

19. Mangin, J. F., "Entropy minimization for automatic correction of intensity nonuniformity," *Proceedings of IEEE Workshop on Mathematical Methods in Biomedical Image Analysis -- MMBIA'00*, pages 162--169, 2000 *IEEE,* 2000. Available: http://brainvisa.info/pdf/mangin-MMBIA00.pdf

20. Wicks, D.G., Barker, G.J., Tofts, P.S., "Correction of intensity nonuniformity in MR images of any orientation," *Magnetic Resonance Imaging*, 11, pp. 183-196, 1993.

21. Narayana, P.A., Brey, W.W., Kulkarni, V., Sievenpiper, C.L., "Compensation for surface coil sensitivity variation in magnetic resonance imaging," *Magnetic Resonance Imaging* 6, pp. 271-274, 1998.

22. Guillemaud, R., "Uniformity correction with homomorphic filtering on region of interest," *IEEE,* 1998. Available: http://ieeexplore.ieee.org/iel4/5852/15601/00723695.pdf?arnumber=723695

23. Parker, J. R., *Algorithms for Image Processing and Computer Vision*, Wiley Computer Pub., 1997.

24. Gonzalez, R. C., Woods, R. E., *Digital Image Processing*, Addison-Wesley, 1992.